Geochemistry, Geophysics, Geosystems®

RESEARCH ARTICLE
10.1029/2024GC011717

Calculating Sedimentation Rates of Oxic Pelagic Clays Using Core Top Thorium Isotopes

Kassandra M. Costa[1], Frantz Ossa Ossa[1,2,3], Ann Dunlea[4], Frank J. Pavia[5], Logan Tegler[4,6,7,8], Maureen Auro[4,8], Morten Andersen[2], and Sune G. Nielsen[1,8,9]

[1]Department of Geology and Geophysics, Woods Hole Oceanographic Institution, Woods Hole, MA, USA, [2]School of Earth and Environmental Sciences, Cardiff University, Cardiff, UK, [3]Department of Earth Sciences, Khalifa University, Abu Dhabi, United Arab Emirates, [4]Department of Marine Chemistry and Geochemistry, Woods Hole Oceanographic Institution, Woods Hole, MA, USA, [5]Department of Oceanography, University of Washington, Seattle, WA, USA, [6]MIT-WHOI Joint Program in Oceanography/Applied Ocean Science & Engineering, Cambridge, MA, USA, [7]Department of Oceanography, School of Ocean and Earth Science and Technology, University of Hawai'i at Mānoa, Honolulu, HI, USA, [8]NIRVANA Laboratories, Woods Hole Oceanographic Institution, Woods Hole, MA, USA, [9]Research Center Pétrographiques Et Géochimiques, Centre National de la Recherche Scientifique, Université de Lorraine, Vandoeuvre lès Nancy, France

Abstract Oxic pelagic clays are an important component of seafloor sediment that may hold valuable information about past ocean chemistry due to their affinity for and accumulation of biogeochemically important metals. We present a new approach to calculating site-specific sedimentation rates (SRs) by comparing authigenic sediment thorium isotope compositions ($^{230}Th/^{232}Th$) to seawater dissolved $^{230}Th/^{232}Th$ in a suite of deep (>3,000 m) pelagic core sites. We extracted the authigenic sediment fraction using an HHAc leach protocol, which major element chemistry (Al, Mn, Fe, Ti) suggested was less affected by lithogenic contamination than the HCl leach. Four different methods were tested for extracting the appropriate initial $^{230}Th/^{232}Th$ from seawater: using either the nearest water column station (methods 1 and 2) or a regionally averaged profile (methods 3 and 4) and using either the bottommost profile measurement (methods 1 and 3) or linear regression of the profile and extrapolation to the seafloor (methods 2 and 4). Method 3 outperformed the other methods in reconstructing previously published SRs from pelagic clays in the North Pacific. The new thorium-based SRs were then combined with estimates from the total sediment thickness on ocean crust and non-lithogenic cobalt accumulation to determine the best estimates for SRs of oxic pelagic clays. The Pacific has the lowest SR (median 0.28 cm/kyr), while the Atlantic is higher (median 0.46 cm/kyr) and the Indian Ocean is highest (median 0.75 cm/kyr). These new estimates are consistent with the expected spatial patterns of sedimentation, but they revise the absolute SR values downward from available gridded SR maps.

Key Points:

- Thorium isotopes can be used to estimate sedimentation rates (SRs) in oxic pelagic clays
- The best seawater approximation of the initial $^{230}Th/^{232}Th$ is the bottommost value of a regionally averaged water column profile
- Median SR in oxic pelagic clays is 0.46 cm/kyr in the Atlantic, 0.28 cm/kyr in the Pacific, and 0.75 cm/kyr in the Indian

Supporting Information:

Supporting Information may be found in the online version of this article.

Correspondence to:

K. M. Costa,
kassandra.costa@whoi.edu

Citation:

Costa, K. M., Ossa Ossa, F., Dunlea, A., Pavia, F. J., Tegler, L., Auro, M., et al. (2025). Calculating sedimentation rates of oxic pelagic clays using core top thorium isotopes. *Geochemistry, Geophysics, Geosystems*, *26*, e2024GC011717. https://doi.org/10.1029/2024GC011717

Received 20 JUN 2024
Accepted 20 DEC 2024

1. Introduction

Pelagic clays, covering nearly half the seafloor (Diesing, 2020; Dutkiewicz et al., 2015), offer a unique archive for reconstructing past marine micronutrient cycling and long-term climate change. Their slow accumulation rates (often less than 1 m/Myr) and oxygenated porewaters (D'Hondt et al., 2015) preserve metals readily scavenged from seawater, including Fe and Mn. Many studies assume that the role of pelagic clays in modulating ocean chemistry will be similar to that of Fe-Mn crusts and nodules (e.g., Dahl et al., 2010; Dickson, 2017; Little et al., 2014, 2020; Ostrander et al., 2017). However, pelagic clay sediments have their own distinct mineralogy that is much more variable than that of Fe-Mn crusts and nodules, and, consequently, they are likely to interact with seawater differently (Fleischmann et al., 2023). Specific investigation into pelagic clays is crucial for understanding how ocean chemistry evolves across long timescales (e.g., >100 kyr) where biological activity, ocean chemistry and nutrient cycling may have varied. One of the first steps toward qualifying the role of pelagic clays is to constrain their mass accumulation rates on the seafloor.

One method of constraining mass accumulation rates (g/cm^2kyr) is to calculate the sediment ages (e.g., kyr), convert the ages to sedimentation rates (SRs) (e.g., cm/kyr), and use some reasonable estimate of sediment density (e.g., g/cm^3). This approach can be challenging in pelagic clays because they typically lack the calcium carbonate necessary to perform conventional dating techniques such as radiocarbon chronology or benthic $\delta^{18}O$ stratigraphy. Furthermore, their accumulation rates are sufficiently slow that radiocarbon dating would be unlikely to produce useful information. Instead, non-carbonate based chronological tools must be used. These may

include magnetostratigraphy (e.g., Opdyke & Foster, 1970), cobalt accumulation rates (Krishnaswami, 1976), ^{230}Th depth profiling (e.g., Costa et al., 2024; Goldberg & Koide, 1962; Ku et al., 1968; Miyake & Sugimura, 1961), biostratigraphy (e.g., Burckle et al., 1980), and authigenic osmium isotope stratigraphy (Peucker-Ehrenbrink et al., 1995). Some of these techniques require intensive laboratory analyses, including multiple measurements along the sediment depth profile. For example, while ^{230}Th depth profiling is well suited to constraining SRs in pelagic clays (Costa et al., 2024), it carries an analytical burden that can be prohibitive for studies that intend to maximize spatial coverage over temporal resolution. Other techniques (e.g., osmium) are insufficiently precise to usefully date sediments at sub-million year timescales, while the efficacy of other techniques has not yet been verified on a global scale (e.g., cobalt). Consequently, marine metal budgets may have to rely on interpolating from gridded SR models onto their core sites or using broad, regionally integrated basinal estimates (i.e., one SR for the whole North Pacific).

In this study, we investigate a novel approach to calculating site-specific SRs in pelagic clays using core top thorium isotopic compositions. Surface sediments were dated by measuring their authigenic (or seawater-derived) ^{230}Th/^{232}Th and comparing it to proximal dissolved ^{230}Th/^{232}Th measurements. This method relies on the theoretical basis that the authigenic component of the sediment inherits its initial thorium isotope ratio from the water column (Costa et al., 2020) and that the measured sediment ^{230}Th/^{232}Th reflects subsequent ^{230}Th decay (∼75.6 kyr half-life; Cheng et al., 2013) as a function of the core top age. This technique leverages the growing availability of dissolved seawater thorium isotope data (Pavia, 2024) and has the advantage of only requiring a single measurement of the core top sediment. We convert the thorium isotope ages to SRs and then compare them with independent SRs calculated by the more established techniques of cobalt accumulation and total sediment accumulation on top of the ocean crust. Finally, we integrate these multi-proxy estimates to provide the best estimates for the SRs of oxic pelagic clays on a global scale. This technique has several uncertainties, including (a) assumption of the seawater ^{230}Th/^{232}Th as the initial value, (b) extrapolating those seawater data onto distal core sites, and (c) efficacy of the isolation of the authigenic component from sediment. As a result, it is best suited to applications for which low precision (e.g., >±25% uncertainty) is acceptable. In the case of, for example, calculating metal fluxes into pelagic clays, even uncertainties of this magnitude can be an improvement over the available alternative methods.

2. Methods

2.1. Site Selection

Sample selection targeted sediment under deep water (generally >4,000 m) in regions that are likely to have predominantly pelagic clay lithologies and high oxygen concentrations (Diesing, 2020; Dutkiewicz et al., 2015). Modern bottom water oxygen concentrations are >140 μmol/kg at all sites (Garcia et al., 2019), and it is not inconceivable that oxygen may reach all the way to the volcanic basement (D'Hondt et al., 2015). Samples from 69 different core sites (Figure 1, Data Set S1) were acquired from the Woods Hole Oceanographic Institution (WHOI) Seafloor Samples Laboratory, Oregon State University (OSU) Marine and Geology Repository, and the University of Rhode Island-Graduate School of Oceanography (URI-GSO) Marine Geological Samples Laboratory. A few of the samples were collected during a DeepGreen Metals Inc. (now called The Metals Company) cruise to the Clarion Clipperton Zone in the Pacific Ocean. Six additional samples were measured and reported in Data Set S1, but they were not interpreted in this study due to shallow water depth (<3,000 m, n = 2), polar location (n = 1), and non-coretop samples (20–22 cm) at sites that have true coretop samples (n = 3).

Different coring devices recover the sediment-water interface with varying degrees of success. Multi-cores are gently lowered into the seafloor, and thus they are the best archive for capturing the precise sediment-water interface. This study used samples from multi-cores where available, but multi-coring in oxic pelagic clay regions has been limited. Instead, many of the samples in this study come from gravity or piston cores, often collected in the 1960s and 1970s. Samples were taken from the shallowest sediment horizon available in the core; sometimes this was indeed 0–1 cm, but at other times it was, for example, 5–6 cm. Furthermore, the high velocity impact of gravity and piston cores typically blows away or disturbs the sediment at the seawater interface, precluding recovery of the truly youngest sediments, even in the 0–1 cm interval. Bioturbation can homogenize the upper ∼10 cm of sediment, integrating the sediment geochemistry and archival record over correspondingly long time periods (>10–100 s kyr). Given these caveats we recognize that most of the samples studied here do not qualify as true core top sediments. Nevertheless, the ultimate objective of calculating oxic pelagic SRs is to

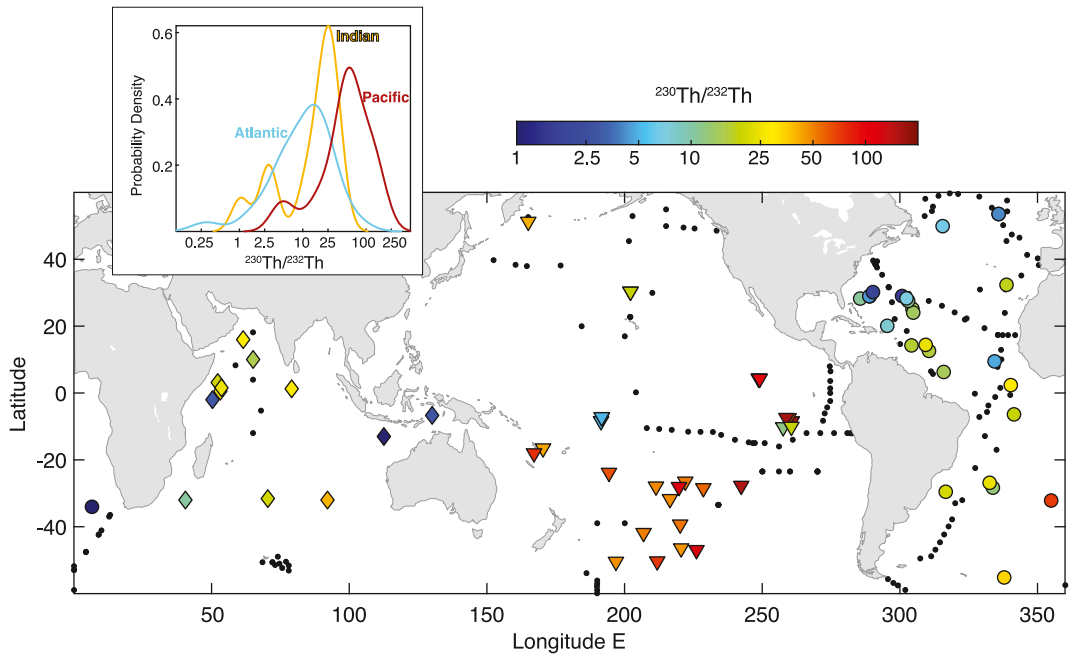

Figure 1. Map of $^{230}Th/^{232}Th$ (dpm/dpm) measured in this study. Colorful symbols are the sediment core tops in this study. Small black dots are locations where there are water column thorium isotope data (Pavia, 2024). (Inset) Probability density distributions of core top $^{230}Th/^{232}Th$ in each ocean basin.

investigate the long term (>100 s kyrs) evolution of seawater chemistry, and for this purpose, SRs integrated over even these long time domains are sufficient and applicable. For simplicity, we use the words "core top" and "surface" to describe our samples because they often represent the youngest material available from pelagic clays.

2.2. Sample Digestions and Leaching

The samples were prepared in the NIRVANA clean laboratory facilities at WHOI. All acids were double distilled in-house and tested for their elemental concentrations before use, with the exceptions of the hydrofluoric acid (HF) and hydrogen peroxide (H_2O_2) (both were Optima Grade, Fisher Scientific). Ultrapure (18.2 MΩ) deionized water (Milli-Q) was used to dilute the acids as needed. The three procedures outlined below were conducted independently on separate sediment aliquots rather than sequentially on a single sediment aliquot. To measure bulk elemental concentrations, about 100 mg of each sample was weighed into an acid-cleaned perfluoroalkoxy (PFA) vial and digested in 1:1 mixtures of concentrated HF and nitric acid (HNO_3) followed by multiple treatments with concentrated hydrochloric acid (HCl) and HNO_3 to achieve complete digestion. A small sub-sample of this digested material was run on an iCAP-Q ICP-MS (Quadrapole Inductively Coupled Plasma Mass Spectrometry, Thermo Fisher Scientific) to obtain elemental concentrations. Next, two different partial digestion (i.e., leaching) procedures were conducted to isolate the seawater-derived, or authigenic, component of the pelagic clays from lithogenic matter. In the first partial digestion ("HCl leach"), approximately 12 mL of 1 M HCl was added to ∼400 mg of powdered sample in an acid-cleaned high-density polyethylene (HDPE) sample vials. These samples were placed on a shaker table at 20°C for 24 hr to allow for exchange between the solution and sediment. The leachate was centrifuged (3,000 rpm for 10 min) until the supernatant was clear, indicating no sediment carryover. Small aliquots were taken for elemental analysis on the iCAP-Q ICP-MS. This "HCl leach" procedure primarily dissolves iron (Fe) oxyhydroxides while leaving lithogenic silicates largely undissolved (Dunlea et al., 2021). In the second partial digestion ("HHAc leach"), approximately 10 mL of 1M hydroxylamine hydrochloride in 25% acetic acid (HHAc) was added to another ∼400–500 mg of powdered sample, which was weighed into an acid-cleaned PFA vial and heated at 90°C for 3 hr, and then it was agitated every 30 min by hand. Samples were removed from the hotplate, cooled, transferred to 15 mL acid-cleaned centrifuge tubes, centrifuged (3,000 rpm, ∼1,500 g) for 5 min, and the supernatant was transferred to new acid-cleaned PFA vials. The sample residue was rinsed with Milli-Q water two times, centrifuged as described above each time, and added to their corresponding leachate PFA vials, being careful not to transfer any of the residual powder. Previous work has

revealed that this procedure primarily dissolves manganese oxides, whereas authigenic clay minerals and lithogenic silicates are largely undissolved (Bayon et al., 2002). Both the "HCl" and the "HHAc" sample leachates were dried down in acid-cleaned PFA vials, redissolved using aqua regia, and heated overnight at 135°C. They were then dried and digested again with 1 mL each of concentrated HNO_3 and H_2O_2, heated at 100°C overnight, and dried down at 135°C. These leach fractions were redissolved in 0.3 M HNO_3 and subsampled for elemental analysis on the iCAP-Q ICP-MS.

2.3. Thorium Chemistry and Measurements

Thorium isotope chemistry and measurements (Data Set S2) were done in the CELTIC laboratory at the School of Earth and Environmental Sciences, Cardiff University, UK. Replicates were conducted on a subset of 19 samples. Thorium separation was performed on the HHAc leachates from WHOI, with aliquots containing at least 5 ng of Th, through a two-step column chemistry using TRU Spec and UTEVA resins, respectively, modified from Potter et al. (2005). The first step utilized Bio-Rad columns filled with ∼1 mL volumes of TRU resin (100–150 μm). Resin cleaning was done using ∼10 mL of a mixed solution of 0.1 M HCl—0.3 M HF, rinsed with 5 mL Milli-Q H_2O, and conditioned with 5 mL of 1.5 M HNO_3. Samples were dissolved in 5 mL of 1.5 M HNO_3 and then loaded onto the columns. Major elements were eluted using two sequential 10 mL additions of 1.5 M HNO_3. Thorium and some other trace elements (e.g., U and REEs) were eluted with 10 mL of 0.1 M HCl—0.3 M HF and collected in 15 ml Teflon PFA vials. Sample splits were then dried down on a hotplate at 120°C. Following this, a mixture of 0.5 mL concentrated HNO_3 and 0.5 mL concentrated H_2O_2 was added to the dried samples and heated at 120°C on the hotplate with closed lids for at least 8 hr to break down any residual organics imparted by the column resin. Afterward, the samples were dried down again and redissolved in 3 N HNO_3 for further purification. Approximately 0.5 mL of UTEVA resin was loaded into shrink-fit Teflon PFA columns and cleaned using the same procedure as the TRU resin. The columns were then conditioned with 5 mL 3 M HNO_3 and the samples were loaded, followed by two sequential 10 mL of 3 M HNO_3 to elute remaining major elements and REEs. Thorium was collected in 15 mL Teflon PFA vials with addition 10 mL of 5 M HCl, then dried down on the hotplate at 120°C, and the same HNO_3-H_2O_2 treatment as after the TRU chemistry was done. Samples were then dissolved in 1 mL of 0.3 M HNO_3 for Th isotope measurements.

Thorium isotope ratio measurements were performed on a Nu Plasma II MC-ICP-MS using a Cetac ARIDUS II desolvating nebulizer sample introduction system with an uptake rate of ∼100 μl min^{-1}. The ^{230}Th was collected in a secondary electron multiplier (SEM) while ^{232}Th, ^{233}U, and ^{236}U were collected in Faraday cups connected with 10^{11} Ω resistors. The $^{230}Th/^{232}Th$ ratios were collected in static mode of 20 integrations of 5 s. Raw counts on the SEM (^{230}Th) varied from 50 to 50,000 cps, and SEM intensity linearity was established from tests running standards over this intensity range. Background was subtracted from 0.3 M HNO_3 blank solution measured for 60 s prior to on-peak measurements. Washout between measurements consisted of 60 s of 0.3 M HNO_3 followed by 120 s of 0.3 M HNO_3 _ 0.03 M HF. Data treatment, converting the background corrected $^{230}Th/^{232}Th$ ratios into fully corrected $^{230}Th/^{232}Th$ ratios, included corrections for (a) mass bias, (b) ^{232}Th tailing contribution on the ^{230}Th mass, and (c) SEM-Faraday cup gain. The mass bias per amu was measured prior to each session using the IRMM ^{233}U–^{236}U double spike and normalizing this to the true number using the exponential mass bias law. The tailing was determined prior to each session by peak scanning down-mass from the ^{232}Th beam in an SEM and interpolate its shape from measurements at 231.05, 230.75 and 229.75 using an exponential fit and applying the contribution at mass 230.04 (^{230}Th). The $^{230}Th/^{232}Th$ ratio was $\sim 0.2 \times 10^{-6}$. We used a ∼1 ppb Th concentration of the Th104 thorium standard with a $^{230}Th/^{232}Th$ ratio of $3.74 \times 10^{-5} \pm 9.5 \times 10^{-8}$ (Innocent, 2008; personal communication) as a primary standard to calculate the SEM-Faraday cup gain. The Th104 standard was measured in between every seven unknown samples and the gain would be applied for each unknown averaging the bracketing Th104 measurements. Secondary standards Th103, Th105 and Th104 at 0.5 and 10 ppb (Innocent, 2008) as well as Bristol Isotope Group standard ThoSi (Hoffmann; personal communication) covering $^{230}Th/^{232}Th$ ratios from 7×10^{-4} to 5×10^{-6} were measured interspersed to check the overall performance (Data Set S3). All measured standards show good accuracy and reproducibility with means 0.1 to 0.6% within expected $^{230}Th/^{232}Th$ ratio and ±2 standard deviation variability from 0.3% to 1.5%. Furthermore, aliquots of the sediment standard Nod-A1 were processed through chemistry and repeatedly measured giving a $^{230}Th/^{232}Th$ ratio of $5.93 \times 10^{-6} \pm 6 \times 10^{-8}$ (2 S.D., $n = 6$). Procedural Th blanks for the sample treatment around the column chemistry contained only 3 ± 1 cps on ^{230}Th. For all apart from one sample, ^{230}Th beams were >140 cps, and so the blank corresponds to 2% or less of the ^{230}Th signal. For sample CHN100 85PG 0–3 cm (average 56 cps on

^{230}Th) the contribution of the blank could be ∼5%. These uncertainties are at a level with little significance for the overall variability of the measured ^{230}Th/^{232}Th. Both ^{230}Th and ^{232}Th are converted to units of disintegration per minute (dpm), and throughout the paper the ^{230}Th/^{232}Th isotope ratio is reported in units of dpm/dpm. All thorium isotope data are reported in Data Set S2.

2.4. Elemental Concentration Measurements

Concentrations of major, minor, and trace elements in the bulk digestions and leachates were performed on an iCAP-Q ICP-MS inductively coupled plasma mass spectrometer (ICP-MS) at WHOI. Concentrations were quantified using standard calibration curves constructed from either serially diluted multi-element standards or USGS reference materials (AGV-2, BHVO-2, W-2, Nod P-1, DNC-1a) that were measured multiple times throughout the sample run, at least before and after sample analyses. Indium was added to all samples and standards to monitor instrument drift. Measurement accuracy was verified via analyses of either USGS reference materials BIR-1 and BHVO-1 run as unknowns (i.e., these were not part of the calibration curves) or measurement of an in-house sediment reference sediment sample. Relative standard deviation (RSD) relative to anticipated values for all the measurements was <10%.

Bulk sediment major element concentrations were measured either via X-ray fluorescence (XRF) or ICP optical emission spectroscopy. The XRF analyses were carried out in the Peter Hooper GeoAnalytical lab at Washington State University using previously described techniques (Johnson et al., 1999). Precision and accuracy for these measurements are better than ∼3% for the most abundant major elements (e.g., Si, Mg, Fe, Ca, Al, and Na). The ICP-OES analyses were performed in the Analytical Geochemistry Facilities at Boston University following flux fusion methods described in Dunlea, Murray, Sauvage, Spivack, et al. (2015). First, 100 ± 0.5 mg of sample powder was combined with 400 ± 0.5 mg of lithium metaborate in an ultrapure graphite crucible and cooked at 1050°C for 10 min. The molten sample was poured into 50 mL of 5% nitric acid and shaken (not stirred) and sonicated until dissolved. The solution was filtered through a 0.45 μm Millex filter unit attached to a syringe and diluted again to a final dilution factor of 1:4,000 by mass prior to analysis. Calibration curves were built with standard reference materials (AGV-1, BCR-2, BIR-1, DNC-1, MAG-1, PACS, W-2) and a blank. Three separate digestions of an in-house pelagic clay sediment standard were analyzed for precision (standard deviation/average), which was determined to be 5% for K_2O and P_2O_5 and 2% or below for the other elements. Standard reference material BHVO-2 was analyzed as unknown and was accurate within precision. All data are reported in Data Set S1.

2.5. Age and SR Calculations

The sediment age can be calculated using the standard radioactive decay equation:

$$\left(\frac{^{230}\mathrm{Th}}{^{232}\mathrm{Th}}\right)_{\mathrm{sediment}} = \left(\frac{^{230}\mathrm{Th}}{^{232}\mathrm{Th}}\right)_{\mathrm{initial}} e^{-\lambda t}$$

where $(^{230}\mathrm{Th}/^{232}\mathrm{Th})_{\mathrm{sediment}}$ is the sediment thorium ratio in the HHAc leachate, λ is the decay constant for ^{230}Th, and t is the sediment age. The $(^{230}\mathrm{Th}/^{232}\mathrm{Th})_{\mathrm{initial}}$ is calculated from the dissolved ^{230}Th/^{232}Th database (Pavia, 2024) using one of the four extrapolation methods described in Section 4.3. This approach assumes that the initial thorium isotope composition is constant over time, which is likely not the case. After conducting sensitivity tests (see Supporting Information S1), a reasonable 25% error on $(^{230}\mathrm{Th}/^{232}\mathrm{Th})_{\mathrm{initial}}$ was propagated with the error on $(^{230}\mathrm{Th}/^{232}\mathrm{Th})_{\mathrm{sediment}}$, which results in age uncertainties (1 sigma) of approximately 30 kyr.

The sediments in this study do not precisely correspond to the "core top" (0–1 cm), and so it would not be unexpected for two adjacent sites sampled at different sediment depths (0–1 cm vs. 8–9 cm) to have ages that differ, even by as much as 100,000 years. Sediment ages are thus converted to SRs (depth/age, in cm/kyr) to mitigate this effect. SRs are then modified to account for the biological mixing of sediment, that is, bioturbation, which on average spans 9.8 ± 4.5 cm (Boudreau, 1994). Bioturbation acts as a low pass filter that averages the chemical properties of sediment (e.g., oxygen isotope composition, Mn concentrations, and age) over a mixed layer depth in the sediment (Trauth, 2013). As a result, the calculated age represents the average age of the mixed layer depth rather than that of the exact interval analyzed, with the result that the single sediment horizon will be biased older

by a factor equivalent to the mixed layer depth. We "unfiltered" the data by multiplying by a factor (unitless) equivalent to the mixed layer depth to account for the smoothing caused by bioturbation.

3. Results

Calcium concentrations in the bulk sediment average 3.68 wt% (median) and range from 0.52 wt% to 34.3 wt% (Figure 2). Silicon concentrations in the bulk sediment average 19.3 wt% (median) and range from 0.81 wt% to 30.0 wt%. Bulk sediment Ti concentrations (median 0.369 wt%) are nearly identical to Ti in the upper continental crust (0.384 wt%; Rudnick & Gao, 2003). In contrast, bulk sediment Al concentrations (median 6.21 wt%) are lower than in the upper continental crust (8.15 wt%; Rudnick & Gao, 2003), and bulk sediment Fe concentrations (median 4.54 wt%) are slightly higher than in the upper continental crust (3.92 wt%; Rudnick & Gao, 2003). Bulk sediment Mn concentrations (median 0.350 wt%) are four times higher than those in the upper continental crust (0.0774 wt%; Rudnick & Gao, 2003). Bulk sediment Th concentrations (median 9.37 ppm) are slightly lower than those in the upper continental crust (10.5 ppm; Rudnick & Gao, 2003).

In the HHAc leach, Al (0.228 wt%), Ti (0.0016 wt%), and Th (0.433 ppm) concentrations are more than an order of magnitude lower than their respective concentrations in the bulk sediment. The percent extraction (Figures 2g–2k), or the amount of an element present in the leach relative to its total concentration in the bulk sediment, averages 4.55% for Al, 0.604% for Ti, and 4.57% for Th (i.e., 95.43% of the Th in the bulk sediment was not removed by the HHAc leach). The HCl leach had higher Al (0.574 wt%), Ti (0.0097 wt%), and Th (0.950 ppm) concentrations than the HHAc leach, but they were still much lower than in the bulk sediment. The percent extraction by the HCl leach is 11.3% for Al, 3.31% for Ti, and 14.5% for Th. Nearly all Ti enrichment factors ($Ti_{EF} = (Ti/Al)_{leach}/(Ti/Al)_{bulk}$) are less than one for both the HCl leach (median $Ti_{EF} = 0.33$) and the HHAc leach (median $Ti_{EF} = 0.11$) (Figure 2l). Median Th enrichment factors ($Th_{EF} = (Th/Al)_{leach}/(Th/Al)_{bulk}$) are similar for both the HCl leach ($Th_{EF} = 1.15$) and the HHAc leach ($Th_{EF} = 1.24$) (Figure 2o).

Both HHAc and HCl effectively leached Mn from the bulk sediment (Figure 2i), with average percent extractions of 85.4% and 53.0%, respectively. As a result, the Mn concentration in the HHAc leach (median 0.275 wt%) is close to that of the bulk sediment, while the Mn concentration in the HCl leach (median 0.148 wt%) is about half of that of the bulk sediment. With the low extraction of Al and the high extraction of Mn, the manganese enrichment factors ($Mn_{EF} = (Mn/Al)_{leach}/(Mn/Al)_{bulk}$) are high for the HCl leach (median $Mn_{EF} = 4.79$) and especially for the HHAc leach (median $Mn_{EF} = 16.6$) (Figure 2m). All Mn_{EF} in the HHAc leachate are greater than 1.

Substantial Fe was leached from the bulk sediment by both HHAc (median extraction 13.2%) and HCl (21.2%) (Figure 2j). Median Fe concentrations are higher in the HCl leach (0.805 wt%) than in the HHAc leach (0.589 wt%), but since the HCl leach also extracted more Al (Figure 2g), the iron enrichment factors ($Fe_{EF} = (Fe/Al)_{leach}/(Fe/Al)_{bulk}$) are lower in the HCl leach (median $Fe_{EF} = 1.69$) than in the HHAc leach (median $Fe_{EF} = 2.86$) (Figure 2n). All but one Fe_{EF} in the HHAC leachates are greater than 1.

Sediment $^{230}Th/^{232}Th$ ranged from 0.300 to 169, with a median value of 21.1 (Figure 1a). On average, $^{230}Th/^{232}Th$ are lowest in the Atlantic ($n = 27$), which has a unimodal distribution with a median of 12.6 (1.33–39.8, 95% confidence interval) (Figure 1b). The North Atlantic (>0°N) tends to have lower $^{230}Th/^{232}Th$ than the South Atlantic, with the exception of CHN115-38PC to the west of the southern tip of Africa, which has the lowest $^{230}Th/^{232}Th$ (0.300) in the entire data set. Yet, just west of this lowest value is the highest $^{230}Th/^{232}Th$ in the Atlantic (70.9) at CHN115-39PC. This proximity between the highest and lowest values cannot be related to greater depth-related ^{230}Th accumulation, as CHN115-39PC is shallower (4,018 m) than CHN115-38PC (5,260 m). The Sargasso Sea (20°–30°N, 55°–71°W, 4,700–5,984 m) contains a notable cluster of low $^{230}Th/^{232}Th$.

The Indian Ocean ($n = 12$) has an overall median value of 20.5; the apparent bimodal distribution with peaks at 2.8 and 27.1 is unlikely to be robust, given the limited number of samples. The two lowest $^{230}Th/^{232}Th$ (1.05–2.88) occur within the Indonesian Seas (20°–30°N, 55°–71°W), despite these cores being the deepest in the basin at 5,222 m (ALL-93-36PG) and 5,467 m (ALL-93-24PG).

The highest $^{230}Th/^{232}Th$ values occur in the Pacific ($n = 30$), with a median of 52.25 (5.10–167.3, 95% confidence interval). The 10 highest $^{230}Th/^{232}Th$ values (71.5–169) in the entire data set occur in the Pacific, with 8 of 10 sites specifically within the South Pacific (MV0502 and KNOX02RR cruises, 23°–50.5°S, 117°–165°W, 3,688–

10.1029/2024GC011717

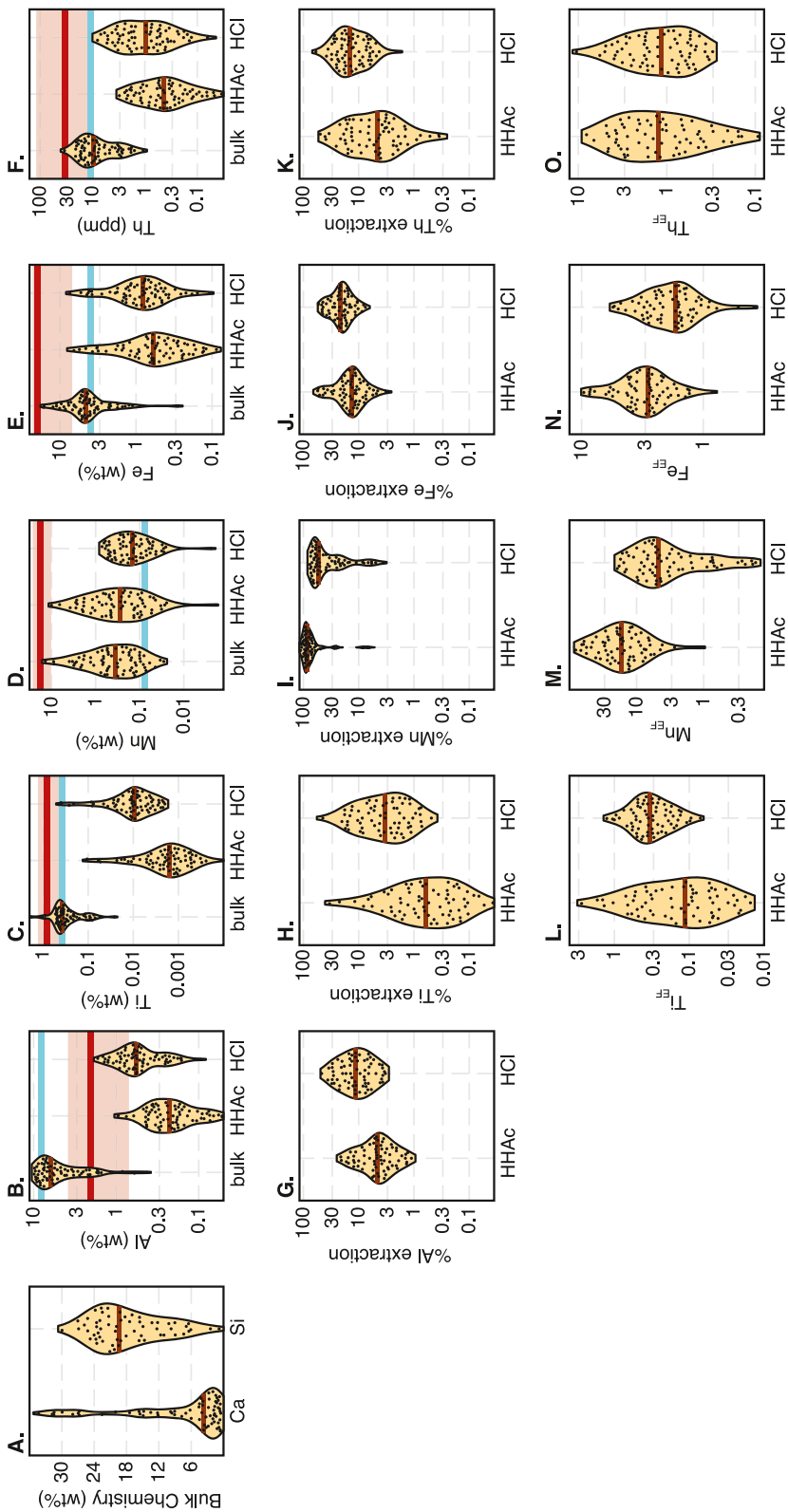

Figure 2. Elemental chemistry of the samples. Brown bars show the median value of each distribution. (a) Concentrations of major biogenic sedimentary phases of the bulk sediment. (b, c, d, e, f) Concentrations of Al, Ti, Mn, Fe, and Th in the bulk sediment, HHAc leach, and HCl leach. Blue line indicates the average concentration in upper continental crust (Rudnick & Gao, 2003). Red shaded region shows the range of concentrations in Fe-Mn crusts (Hein et al., 1999; Mikhailik et al., 2023), with the red line at the median. (g, h, i, j, k) Extraction of Al, Ti, Mn, Fe, and Th into the HHAc leach and HCl leach relative to the bulk sediment. (l, m, n, o) Enrichment factors (EF) of Ti, Mn, Fe, and Ti in the HHAc leach and HCl leach relative to the bulk sediment. All elemental data are provided in Data Set S1.

5,984 m). The lowest $^{230}Th/^{232}Th$ values in the Pacific (4.1–5.2) occur within CHN100 cores in the Eastern Equatorial Pacific (7.2°–8.4°S, 168°W, 5,026–5,724 m). Because not many samples from the North Pacific Ocean were included in this study, we refrain from making generalizations about this region.

4. Discussion

4.1. Potential Sources of Th in Pelagic Clays Based on Bulk Element Concentrations

Oxic pelagic sediments contain a variety of sedimentary components, including aluminosilicate dust, volcanic ash, hydrothermal particles, biogenic particles, and authigenic phases (Dunlea, Murray, Sauvage, Pockalny, et al., 2015; Dunlea, Murray, Sauvage, Spivack, et al., 2015; Kyte et al., 1993; Leinen, 1987). These regions tend to have low concentrations (<10 wt%) of biogenic particles, such as calcium carbonate ($CaCO_3$) and opal (SiO_2) (Hayes et al., 2021), and the majority of our samples are consistent with this expectation. Most Si in oxic pelagic sediments is non-biogenic and derived from volcanic and eolian sources (Dunlea, Murray, Sauvage, Pockalny, et al., 2015; Kyte et al., 1993), and no samples contain high enough concentrations of Si to indicate the presence of significant biogenic SiO_2 (Figure 2a). Assuming that all bulk Ca is derived from $CaCO_3$, then at most 10 samples exhibit high abundances of $CaCO_3$ (>50 wt%) (Figure 2a).

Of our pelagic clay samples, 91.3% of them have more Mn than typical upper continental crust (Rudnick & Gao, 2003), suggesting enrichment of Mn from seawater. The observed high Mn (and to some extent Fe) concentrations in the bulk sediment (Figures 2d and 2e) are consistent with expectations for oxic pelagic sediments. Slow SRs in pelagic clay lithologies allow ample time for metals to be scavenged from seawater and enriched in the sediment. Sometimes Mn concentrations can be as high as 10 wt% in slowly accumulating pelagic clays (Dymond et al., 1973; Marchig et al., 1982). Hydrothermal vents are the primary source of particulate and dissolved Mn in most regions of the deep sea, but seawater Mn can also be supplied from eolian sources, river input, or reductive or nonreductive remobilization from the sediment (Bostrom et al., 1973; Van Hulten et al., 2017). Over time, the Mn in seawater accumulates in or on the sediment as coatings on other particles, crusts, nodules, and microparticles (Dymond et al., 1973; Marchig et al., 1982; Rudnick & Gao, 2003; Uramoto et al., 2019). Fe and especially Mn have high partition coefficients for Th, and they likely scavenge seawater Th close to the site of sediment deposition (Hayes, Anderson, Fleisher, Vivancos, et al., 2015). Thus, the Fe- and Mn-oxides are most likely to retain the Th used to calculate the average amount of time passed since the sediment was deposited on the seafloor.

In contrast to Fe-Mn rich sedimentary components, aluminosilicate dust and volcanic ash (hereafter referred together as "lithogenic") contain high concentrations of Th that typically have low $^{230}Th/^{232}Th$ (0.797) using average upper continental crust concentrations of ^{232}Th and ^{238}U and assuming that ^{230}Th is in secular equilibrium with ^{238}U (Rudnick & Gao, 2003). The incorporation of lithogenic material has the potential to affect calculated Th ages by skewing them too old. Bulk contents of Al (Figure 2b) and Ti (Figure 2c) that equal or even exceed those of the upper continental crust (Rudnick & Gao, 2003) indicate that the lithogenic component of the sediment is substantial in the majority of our samples. To isolate seawater-derived Th from lithogenic Th, we applied two different leaching procedures that preferentially extract the authigenic components of the sediment.

4.2. Efficacy of Leaching Procedures to Isolate Authigenic Thorium

Numerous leaching procedures have been developed in attempts to separate authigenic (i.e., previously dissolved in seawater) from detrital (i.e., mineral-hosted) sedimentary components. The specific chemical procedures vary depending on the target authigenic phase, but they often involve HCl (Goldberg & Koide, 1962; Raiswell et al., 1994; Robinson et al., 2008) and/or HHAc (Bayon et al., 2002; Chester & Hughes, 1967; Gutjahr et al., 2007), applied at a range of concentrations, durations, and temperatures. In this study, we have followed the leaching protocols of Bayon et al. (2002), which were originally designed for Sr and Nd isotopes and have since been adapted for other isotope systems as well (e.g., thallium; Nielsen et al., 2005). We have not conducted new method development, but below we evaluate the efficacy of the HCl leach and HHAc leach specifically for thorium in our pelagic clay samples.

In practice, the HCl leach is designed to dissolve insoluble Fe oxyhydroxides (ferrihydrite and pyrite, although not goethite or hematite (Raiswell et al., 1994)), and in our samples the extraction of Fe is nearly twice as high in the HCl leach (21.2% of the bulk Fe) compared to the HHAc leach (13.2% of the bulk Fe) (Figure 2j). The high Fe

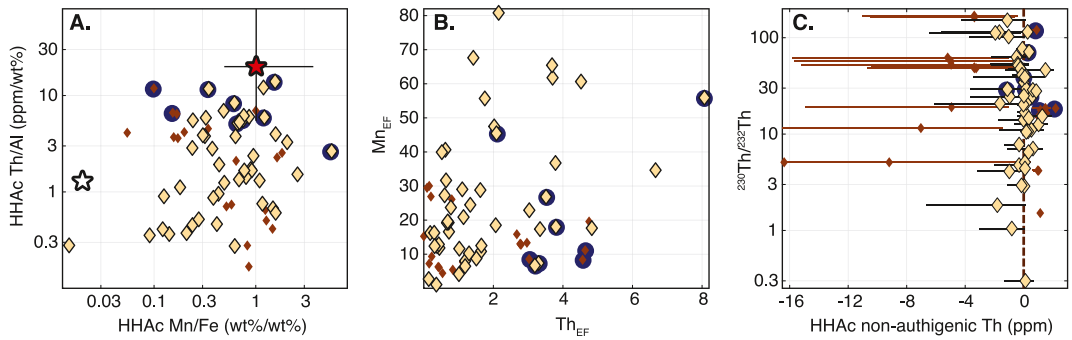

Figure 3. Geochemical evidence for lithogenic contributions in the HHAc leachate. (a) Mn/Fe in the HHAc leach versus the Th/Al in the HHAc leachate. White star indicates the composition of average upper continental crust (Rudnick & Gao, 2003). Red star and black bars show the range of Mn/Fe and Th/Al found in Fe-Mn crusts (Hein et al., 1999; Mikhailik et al., 2023). (b) Th_{EF} and Mn_{EF} of the HHAc leach relative to the bulk composition. (c) Non-authigenic Th content in the HHAc leach versus the Th isotopic composition of the HHAc leach. In all panels, the small dark brown symbols identify the samples for which the non-authigenic Th content is statistically distinct from zero. Navy circles indicate samples with bulk $CaCO_3$ contents greater than 50 wt%.

extraction is consistent with the HCl attacking authigenic Fe minerals in our samples. At the same time, the extraction of Th is more than three times higher in the HCl leach (14.5% of the bulk Th) compared to the HHAc leach (4.6% of the bulk Th) (Figure 2k). Similarly high extraction of other lithogenic elements like Al (11.3% in HCl vs. 4.5% in HHAc) and Ti (3.3% in HCl vs. 0.6% in HHAc) suggest the possibility of lithogenic contamination of the HCl leach, in contrast to two previous studies that used HCl leachates to extract authigenic Th. Robinson et al. (2008) corroborated an authigenic Th signal in HCl leachates with ($^{234}U/^{238}U$) activity ratios equivalent to that of seawater (1.146) in all samples except one—the pelagic clay ($^{234}U/^{238}U = 1.73$). A study exclusively on pelagic clays (Goldberg & Koide, 1962) found that ~70% of the bulk thorium was extracted in the HCl leach, a yield so high it seems improbable without containing some lithogenic contamination. One possibility is that the HCl leaching procedure may be too aggressive for pelagic clay sediments, but it may be acceptable for other sediment compositions, such as those in Robinson et al. (2008). Unfortunately, neither of these studies included major or trace element concentrations, and so the relationship between sediment composition and lithogenic contamination of the HCl leach cannot be explicitly defined. Given the uncertainties in using HCl to extract an authigenic thorium signal, we did not pursue thorium isotope measurements on the HCl leachates.

Manganese oxides (e.g., todorokite, hexagonal birnessite, vernadite) are important sedimentary components because they have a high affinity for scavenging trace metals from seawater (Dymond et al., 1973), including thorium (Hayes, Anderson, Fleisher, Vivancos, et al., 2015). The HHAc leach is designed to preferentially attack Mn oxide minerals relative to lithogenic phases, Fe oxyhydroxides, and authigenic clay minerals (Bayon et al., 2002; Chester & Hughes, 1967). This effect is clearly observed in our samples, for which the HHAc leach successfully extracted, on average, ~85% of the total Mn in the bulk samples. Relatively low extraction of Ti (0.6% of bulk Ti) and Al (4.5% of bulk Al) suggest that the likelihood of lithogenic contamination of the HHAc is lower than it is in the HCl leach. However, incorporation of any lithogenic material could bias the ^{232}Th concentrations too high and the $^{230}Th/^{232}Th$ too low, resulting in calculated ages that are too old compared to the true age of the sediment. If the lithogenic Th comprises more than 25% of the total Th in the HHAc leach, the calculated ages will be no longer be valid (see Supporting Information S1).

The potential for incorporation of lithogenic material into the HHAc leach can be diagnosed by several different lines of evidence. High Mn_{EF} in the HHAc leach indicate that the fraction of Mn oxide extracted is large relative to the lithogenic component of the sediment. In contrast, low Mn_{EF} might indicate that a relatively high fraction of lithogenic material was extracted by the HHAc leach. Because all samples have Mn_{EF} greater than 1 (median 16.6) (Figures 2 and 3), it appears that the HHAc leach has successfully attacked the Mn oxides over the lithogenic component in the sediment. When combined with high Mn_{EF}, a Th_{EF} greater than 1 is also consistent with successful preferential leaching of the Mn oxides over the lithogenic component in the sediment (Figure 3). The Th/Al of UCC is only 1.29 (ppm/wt%; Rudnick & Gao, 2003), whereas the median Th/Al of Fe-Mn crusts is 20.0 (ppm/wt%; Hein et al., 1999; Mikhailik et al., 2023). A successful HHAc leach of the Mn oxides would thus increase both Th_{EF} and Mn_{EF}, as evident in our samples (Figure 3b).

The authigenic and lithogenic Th components can be semi-quantified by assuming a two-endmember mixture of UCC and Fe-Mn crusts in the sediments. One common approach would be to assume all Ti (or Al) in the HHAc leach was lithogenic in origin and then to multiply by the UCC Th/Ti to estimate the amount of lithogenic Th. However, the assumption that all Ti (or Al) in the HHAc leach is lithogenic is likely incorrect—Fe-Mn crusts contain more than double the Ti (0.80 wt%; Hein et al., 1999; Mikhailik et al., 2023) than UCC (0.38 wt%; Rudnick & Gao, 2003). Instead, we take the opposite approach: assume all Mn in the HHAc leach is authigenic in origin and then multiply by the Fe-Mn crust Th/Mn (median 1.87 ppm/wt%, range 0.39–5.67 ppm/wt%) to estimate the amount of authigenic Th. Subtracting this from the measured Th gives the non-authigenic (ostensibly lithogenic) Th present in the leach (Figure 3c). This approach is preferred because the Mn content of Fe-Mn crusts (17.8 wt%) is two orders of magnitude greater than the Mn content of UCC (0.08 wt%), and so the simplification of assuming that all Mn in the leach is coming from the Mn oxides is not unreasonable. Due to the large range in Fe-Mn crust Th/Mn (0.39–5.67 ppm/wt%), the resulting non-authigenic Th estimates are not precise, and so the lithogenic risk is semi-quantitatively identified as those samples for which the calculated non-authigenic Th range does not overlap with zero.

The majority of samples ($n = 48$, or 68%) have non-authigenic Th that is indistinguishable from zero, consistent with minimal liberation of the lithogenic material in the HHAc leach (Figure 3). Nine samples have positive non-authigenic Th present in the leach, and they come predominantly from the Atlantic ($n = 6$), but also from the Pacific ($n = 2$) and the Indian ($n = 1$) (Figure S1 in Supporting Information S1). These sediments are distinct for their relatively low bulk Mn (median 0.10 wt%, compared to 0.32 wt% in the samples with ∼0 non-authigenic Th) and HHAc Mn (0.09 wt%, compared to 0.26 wt%). They also have a high Th extraction (16%, compared to 4.3%) that does not coincide with a similarly high Mn extraction (90.5%, compared to 83.5%). Altogether, the excess Th independent of Mn strongly suggests that these samples are affected by lithogenic contamination of the HHAc leach, which has likely caused the depression of $^{230}Th/^{232}Th$ (median 16.5) compared to samples with ∼0 non-authigenic Th (median $^{230}Th/^{232}Th$ of 24.6). The leaching procedure followed here was designed for sediments with high Fe-Mn components (Bayon et al., 2002), and it may not be appropriate in sediments with low Mn contents, in which it is possible that the leach strength and duration may be too aggressive. This finding is corroborated by a previous study on low Mn sediments (median 0.0113 wt%) from the Atlantic (Gutjahr et al., 2007) in which Th extraction into the HHAc was high (median 14.1%) and nearly 100% non-authigenic (Figure 3c; Figure S3 in Supporting Information S1). Thus, we do not recommend the HHAc leach approach for extracting authigenic signals in low-Mn sediments, and we exclude these nine samples from any further interpretation.

We can also assess whether the leaching procedure was effective in isolating the authigenic component in a $CaCO_3$ rich sediment matrix. High $CaCO_3$ samples were designated as those with Ca content greater than 21.5 wt% (assuming no lithogenic Ca, ∼50 wt% $CaCO_3$). Of those 10 samples, seven also have low Mn content (bulk Mn < 0.25 wt%). Extractions of Al, Fe, Mn, Ti, and Th in the HHAc leachate relative to the bulk were all higher in the high-$CaCO_3$ samples relative to the low-$CaCO_3$ samples. Most notably, Th extraction was more than 5 times higher at 22% extraction (median) in the high-$CaCO_3$ samples compared to 4.12% (median) in low-$CaCO_3$ samples. Three of the sites have positive non-authigenic Th, indicating lithogenic contamination as discussed above (Figure 3c), and the remaining sites are indistinguishable from zero. As a result, we do not resolve a conclusive bias in authigenic extraction for samples with high $CaCO_3$. Future work leaching high $CaCO_3$ sediment could provide more insight into the feasibility of extracting authigenic signals, but for the purposes of chronology, the availability of more reliable chronometers (^{14}C, $\delta^{18}O$) disincentivizes further development of a Th based dating technique in $CaCO_3$-rich sediment.

Twelve samples have negative non-authigenic Th, suggesting that the endmember Th/Mn from Fe-Mn crusts results in an overestimation of authigenic Th. All of these samples come from the Pacific (Figure S1 in Supporting Information S1), and the majority are located within the hydrothermal plume from the East Pacific Rise. These sediments are distinct for their high bulk Mn (median 2.86 wt%, compared to 0.32 wt% in the samples with ∼0 non-authigenic Th) and HHAc Mn (2.66 wt%, compared to 0.26 wt%). Their Th extraction is not exceptional (2.4%, compared to 4.3%) but the Mn extraction is near complete (93.5%, compared to 83.5%). The combination of high Mn relative to Th and the location suggest that the HHAc leach may be incorporating hydrothermal material, rather than being at risk for lithogenic contamination. The Th/Mn of hydrothermal particles is considerably lower (median 0.04, range 0.01–0.17; Lam et al., 2018; Pavia et al., 2018) than that of Fe-Mn crusts, and using the hydrothermal Th/Mn range corrects the calculated non-authigenic Th to be indistinguishable from

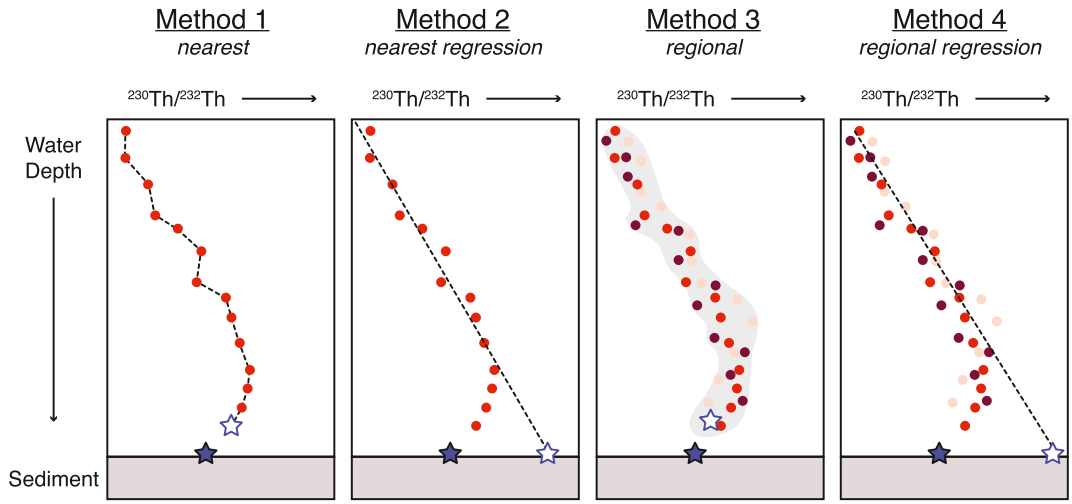

Figure 4. Schematic of four different methods for determining the initial $^{230}Th/^{232}Th$ from seawater profiles. Colored circles indicate seawater measurements. Solid blue star is the $^{230}Th/^{232}Th$ in coretop sediments. Open blue star is the initial $^{230}Th/^{232}Th$ derived from the seawater profiles. Method 1 uses the deepest seawater measurement from the closest station. Method 2 uses a linear regression of the seawater measurements from the closest station to extrapolate an initial value at the sediment surface. Method 3 is the same as Method 1 except that it uses the average seawater value from all stations within the same biogeochemical province rather than a single profile. Method 4 is the same as Method 2 except that it uses the average seawater value from all stations within the same biogeochemical province rather than a single profile.

zero at 10 out of 12 sites. Fortunately, while hydrothermal particles are strong scavengers of Th, they do not fractionate Th isotopes and thus retain the seawater $^{230}Th/^{232}Th$ (Pavia et al., 2018). Therefore, we included these samples in subsequent analyses with extra scrutiny for potential anomalies from the non-hydrothermally affected samples.

4.3. Calculating SRs Using Water Column $^{230}Th/^{232}Th$

To calculate ages and then SRs from the core top $^{230}Th/^{232}Th$ values, some estimate of the initial $^{230}Th/^{232}Th$ at the seafloor must be assumed. Thorium-230 is produced throughout the water column by the radioactive decay of U, and it rapidly adsorbs onto sinking particles (Bacon & Anderson, 1982). There is a linear increase in dissolved and particulate ^{230}Th concentrations with water depth that is primarily attributed to reversible scavenging, a process in which adsorbed and dissolved ^{230}Th are continuously exchanging as particles settle through the water column (Bacon & Anderson, 1982; Nozaki et al., 1987). Because the sediment accumulating on the seafloor is ultimately derived from particulates settling out of the water column, the $^{230}Th/^{232}Th$ of these particulates may provide an estimate of the initial $^{230}Th/^{232}Th$ (Pavia, 2024). However, particulates contain both lithogenic and adsorbed thorium components, making their $^{230}Th/^{232}Th$ ratio comparable to that of the bulk sediment than to the Th in the HHAc leachate. Dissolved thorium isotope ratios likely provide a more relevant baseline for the authigenic $^{230}Th/^{232}Th$ composition recorded in the Mn oxide phases and leached from the sediment by HHAc. In this study, we use the abundant and spatially distributed dissolved $^{230}Th/^{232}Th$ measurements (Pavia, 2024) to approximate the initial ratio in sediment leachates. A previous study of relatively young sediments (1,000–8,870 years old) found reasonable agreement (R^2 = 0.45) between dissolved $^{230}Th/^{232}Th$ and core top bulk sediment $^{230}Th/^{232}Th$ (Rowland et al., 2017), but true validation of this technique would require comparison of collocated dissolved $^{230}Th/^{232}Th$ and the authigenic (HHAc-leached) component of core top sediment that has been independently constrained to zero age, which, although widely assumed, is often rare in deep pelagic sediments (e.g., >2,000 m). The dating approach presented here is derived from the theoretical behavior of Th in seawater (e.g., Bacon & Anderson, 1982), and in the absence of empirical validation, we acknowledge that large uncertainties on both the ages and the SRs are warranted.

We use four different methods to estimate the initial $^{230}Th/^{232}Th$ for the authigenic component of pelagic clays (Figure 4): (1) *Nearest* = extracting the bottommost dissolved $^{230}Th/^{232}Th$ from the nearest water column profile; (2) *Nearest regression* = extrapolating to the seafloor using a linear regression of dissolved $^{230}Th/^{232}Th$ from the nearest water column profile, (3) *Regional* = extracting the bottommost dissolved $^{230}Th/^{232}Th$ from averaged

regional water column profiles, and (4) *Regional regression* = extrapolating to the seafloor using a linear regression of dissolved $^{230}Th/^{232}Th$ from averaged regional water column profiles. The motivation for conducting both bottommost (methods 1 and 3) and regression (methods 2 and 4) approaches is that dissolved $^{230}Th/^{232}Th$ does not always increase linearly with depth all the way to the seafloor, as theoretically predicted. The motivation for comparing nearest (methods 1 and 2) and regional (methods 3 and 4) methods is that the strictly nearest water column profile may not be representative of the conditions observed at the sediment sites since water column stations and the sediment sites are generally not co-located (Figure 1). As an alternative, we generate regional profiles by averaging all the profiles within the site's Longhurst province (Longhurst, 1995), and use this averaged profile to determine the initial $^{230}Th/^{232}Th$ from the bottommost value (method 1, 3) or linear regression value (method 2, 4). Longhurst provinces are designed to reflect regions with similar biogeochemical and physical properties at the surface, in the water column, and along the seafloor (Longhurst, 1995), such that the mechanisms controlling dissolved thorium concentrations and isotopic compositions should be relatively homogenous. As a consequence, the most representative water column profile may not be the one closest to the sample site but the one(s) within the same biogeochemical regime.

Before applying this new technique (hereafter called the "seawater technique") to our new core top locations, we first conducted a proof of concept test using a suite of pelagic clay sites in the North Pacific for which SRs have been previously calculated using the more traditional ^{230}Th profiling technique (Costa et al., 2024). Seawater initial $^{230}Th/^{232}Th$ was estimated using the four methods described above, and the shallowest sediment depth $^{230}Th/^{232}Th$ measurement at each site was used for the SR calculation. Only sites with quality scores of A, B, or C were included in the comparison (Costa et al., 2024), and of those, only sites with SR calculations from all four methods were included in the final comparisons ($n = 21$). The correlations were estimated using 10,000 iterations of linear regression using bootstrapping of each sample within its uncertainty domain. For the Th downcore profiling approach, a full probability distribution ($n = 3{,}000$) was previously calculated using Bayesian statistical techniques (see Costa et al., 2024), and each iteration randomly sampled from that population for each site. The seawater technique only calculates one SR (with an error of ~25%), and so each iteration sampled randomly from a normally distributed population using the SR value as the mean and the uncertainty as the standard deviation. The SR probability distribution is almost certainly not normally distributed, but in the absence of further constraints, we default to this simplest option.

In general, all four methods in the seawater technique produced SRs that were positively and linearly correlated (all $p < 0.017$) with the previously published SR estimates (Figure 5). Expecting perfect agreement between the two dating techniques may not be realistic, and indeed the seawater technique SRs tend to underestimate the SRs from Th profiling. Method 1 and method 2 resulted in SRs that were only 20%–30% of the previously published SRs from ^{230}Th depth profiling. Method 3 and method 4 resulted in higher SRs, but they were still only 40%–60% (median) of the previously published SRs from ^{230}Th depth profiling. Only in method 3 could the seawater technique SRs achieve unity with previously published SRs within the 95% confidence interval. The better performance of methods 3 and 4 over methods 1 and 2 indicates that using regionally integrated seawater profiles provides more relevant initial $^{230}Th/^{232}Th$ values for calculating core top sediment age, at least in the North Pacific. The difference between the two spatial parameterizations would be most critical for cores on the cusp of two different Longhurst provinces. For example, for a core in the subpolar gyre, it would be more effective to reference more distant seawater profiles that reflect similarly high fluxes, biogenic particle compositions, and boundary currents than it would be to use a closer seawater profile coming from the subtropical gyre. In cases where the nearest profile is located within the same Longhurst province as the site, there is little to no practical change in the resulting SR. The main drawback of using the regionally integrated methods is that not all Longhurst provinces currently contain water column profiles, but this will improve as future work increases the spatial coverage of water column profiles. For the purposes of this study, the better agreement with previously published SRs outweighs the number of datapoints for which no SR can be calculated, and so we proceed to focus on methods 3 and 4.

Method 4 consistently returns lower SR than method 3. As shown schematically in Figure 4, extrapolating a linearly regressed seawater profile down to the seafloor results in an assumed initial $^{230}Th/^{232}Th$ that is higher than using the bottommost value, which translates to older core top ages and lower SRs. In some locations, including the North Pacific, the $^{230}Th/^{232}Th$ trend increases linearly with water depth until some 100s of meters above the seafloor, at which point the trend reverses such that $^{230}Th/^{232}Th$ decreases with increasing water depth (e.g., Hayes, Anderson, Fleisher, et al., 2013; Hayes, Anderson, Fleisher, Huang, et al., 2015; Hayes, Anderson,

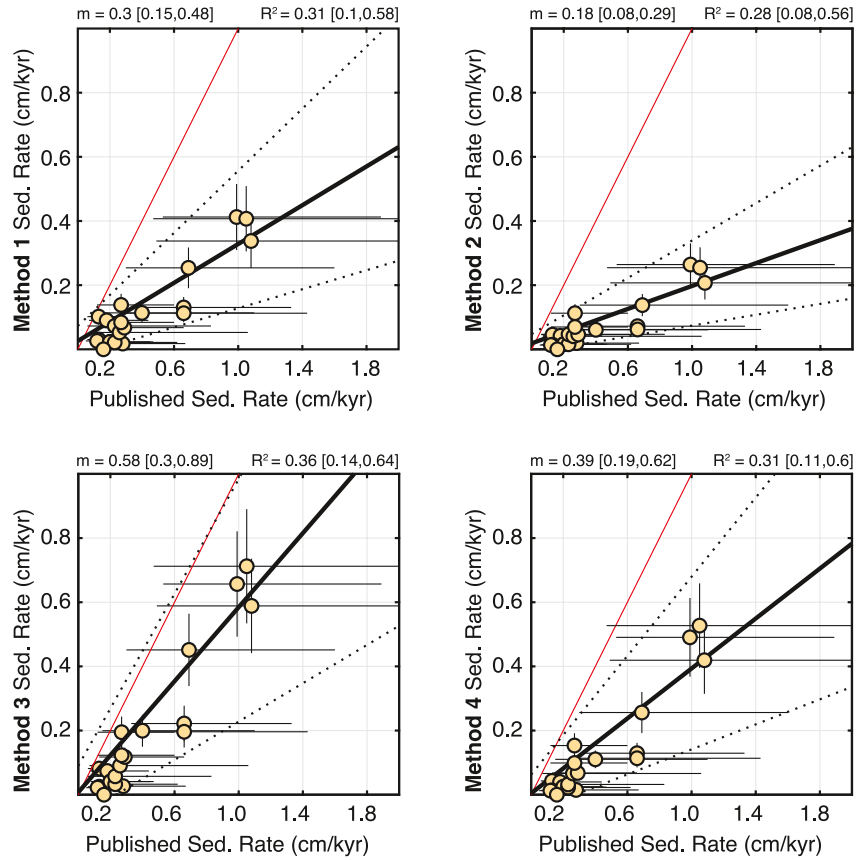

Figure 5. Comparison of the seawater sedimentation rate methods with previously published estimates from the downcore ^{230}Th profile method (Costa et al., 2024). Slope (m) and correlation coefficient (R^2) are reported as medians with the 95% confidence limits in brackets. Red line is 1:1, black line is the best fit, and dotted lines represent the 95% confidence limits on the best fit.

Jaccard, et al., 2013; Okubo et al., 2012). This reversal may reflect benthic nepheloid layers, regions of high suspended sediment load near the seafloor, often related to high current velocities (Gardner et al., 2017; McCave, 1986). Nepheloid layers may also entrain allochthonous sediment of different age and composition than the underlying sediment that we are trying to date (see Costa et al., 2020, Section 6.2, for more details about the potential effects of nepheloid layers on Th isotope systematics). The timescales and frequencies of intermittent nepheloid layers resuspending and resettling sediment is poorly constrained, and thus whether or not dissolved ^{230}Th/^{232}Th within a nepheloid layer is the best initial value to use for age determination could not be determined a priori. The better agreement of method 3 with the previously published SR (Figure 5) indicates that the effects of nepheloid layers on the bottommost value may be minimal relative to the initial ^{230}Th/^{232}Th that the core top sediment "sees," at least in comparison to the alternative linear extrapolation as we have parameterized it here. The underestimation of method 3 relative to previously published values suggests that even the bottommost seawater ^{230}Th/^{232}Th may be too high, and it is possible that a nonlinear model that captures the curvature of the seawater profile may extrapolate to a lower value than either method 3 or method 4, resulting in lower ^{230}Th/^{232}Th relative to the core top value, younger ages, and thus higher SRs. For the purposes of this study, we take the seawater ^{230}Th/^{232}Th at face value and interpret the method 3 as representing the minimum SR.

The SR distributions for all of our core tops are shown for each of the four methods (Figure 6a), and the ocean-specific distributions (Figure 6b) and map (Figure 6c) are shown for method 3. Similar plots for methods 1, 2, and 4 are available in Figure S3 in Supporting Information S1. Method 1 has the highest median SR (0.24 cm/kyr), while method 2 has SRs half as low (0.12 cm/kyr). The same pattern emerges when using regionally integrated (^{230}Th/^{232}Th)$_{initial}$ values: method 3 (regional) has a higher median SR (0.19 cm/kyr) than method 4 (regional regression; median SR 0.13 cm/kyr). Focusing in on method 3 (Figures 6b and 6c), SRs are lower in the Pacific

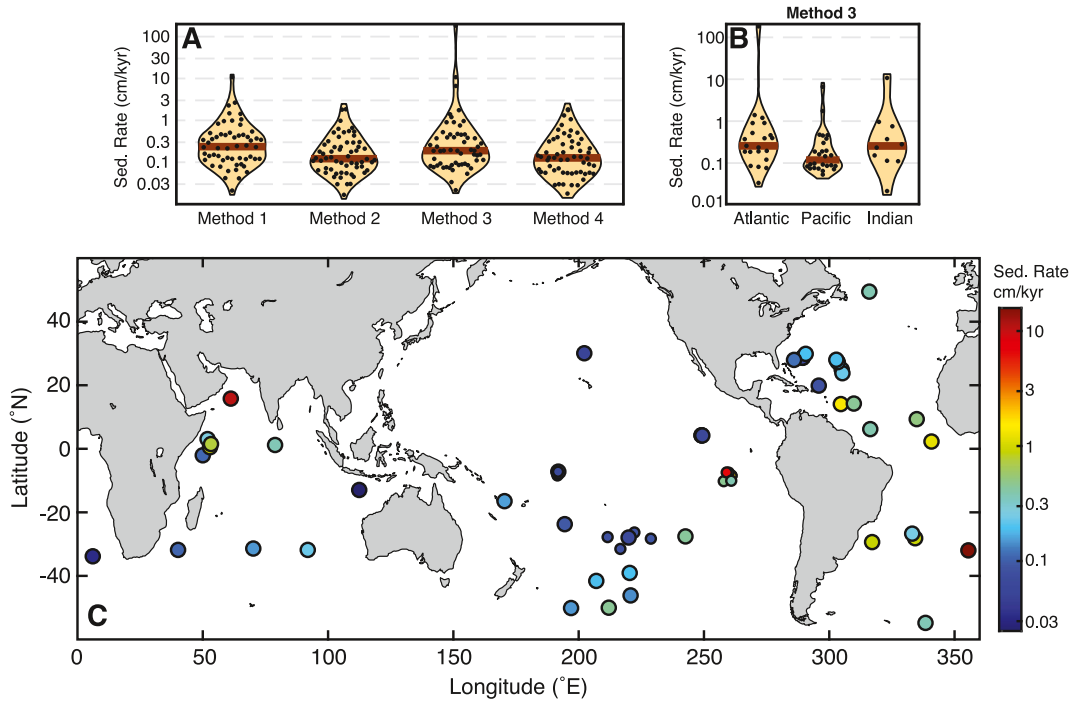

Figure 6. Sedimentation rates (SRs) calculated using the new seawater Th methods. (a) Distributions of SR at all core sites based on the four different methods for calculating initial $^{230}Th/^{232}Th$. (b) Ocean-specific distributions of SR calculated using method 3. (c) Map of SR calculated using method 3. All distributions in A and B incorporate the errors on the data. Cores with negative non-authigenic Th (see Section 4.2) are shown with smaller symbols. Maps and ocean-specific distributions are provided for methods 1, 2, and 4 in Figure S3 in Supporting Information S1.

(median 0.12 cm/kyr) than in the Atlantic (median 0.35 cm/kyr) and Indian (median 0.37 cm/kyr). In the Atlantic, the Sargasso Sea (20°–30°N, 285°–305°E, 4,705–5,984 m) has relatively uniform SRs ranging from 0.08 to 0.24 cm/kyr. Similarly low and uniform SRs (0.07–0.20 cm/kyr) can be found across an even broader region in the South Pacific (7°–40°S, 190°–230°E, 4,056–5,742 m).

There is one extremely high SR of 183 cm/kyr at site CHN115-39PC (32.2°S, 355°E, 4,018 m) in the South Atlantic. The other four cores within the Longhurst province (similar latitude, at 315°E, 330°E, and 6.5°E) all have more realistic SRs for pelagic clays (0.03–0.90 cm/kyr), suggesting that the issue is not with the modeled initial $^{230}Th/^{232}Th$ value but with the specific core itself. CHN115-39PC contains the highest $CaCO_3$ content (85 wt%) in the data set, and it does not contain any non-authigenic Th distinguishable from zero. It did have the lowest bulk ^{232}Th concentration, but the Th extraction efficiency was high (~40%) so that the Th concentration in the leach was not uniquely low. There are no particular "red flags" besides the high $CaCO_3$ content, and so it is possible (though unlikely) that the SR is real.

4.4. SR Comparisons

Next, we will compare the new SRs (from method 3) with SRs calculated using independent methods (Figure 7). First, SRs can be estimated based on the age of the ocean crust (Müller et al., 2008) and the thickness of the overlying sediment (Straume et al., 2019). Crustal SRs are calculated on a gridded field that is then interpolated onto the individual sites in this study, and errors are estimated by the standard deviation of crust SRs within a 10 km radius of the core site (Data Set S4). Crust SR provides a baseline constraint on the "all time" mean SR integrated over 10s or 100s of millions of years. Consequently, it incorporates SR variability that occurred outside the time domain (millions of years) of the ^{230}Th SR reconstructions (~100s of thousands of years). For example, discontinuous sedimentation caused by, for example, redistribution of sediment by changing ocean currents over geologic timescales (Dutkiewicz & Müller, 2022) may have introduced hiatuses into the sedimentary record. As a result, the crustal age could overestimate the accumulation time necessary to generate the thickness of the

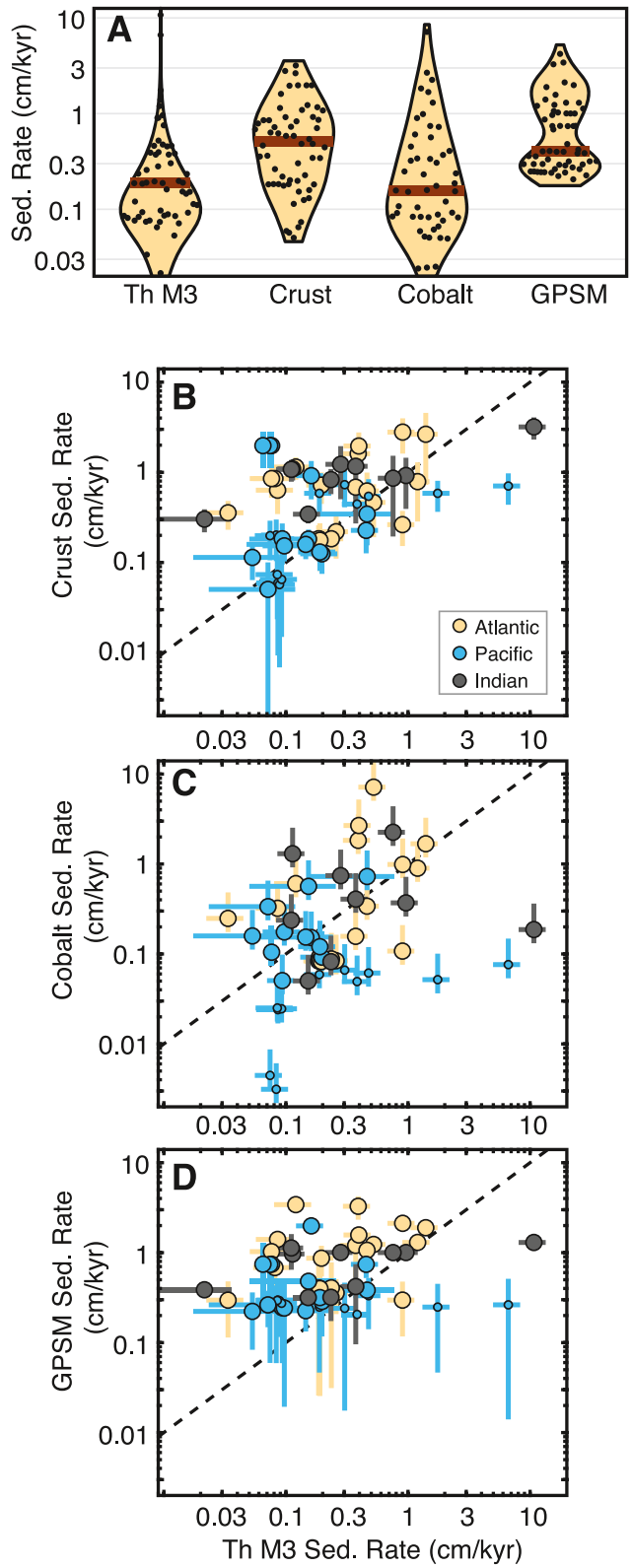

Figure 7.

overlying sediment column and bias crustal SR lower than ^{230}Th SR. On the other hand, newly formed ocean crust is often proximal to hydrothermal activity that can cause substantial deposition of Fe and Mn rich minerals, and young hot ocean crust may have been shallower than the carbonate compensation depth, allowing the accumulation of calcium carbonate that would not be possible later as the crust cools and sinks with increasing distance from its source mid-ocean ridge. Both these effects could bias crustal SR to be higher than ^{230}Th SR, which would not encompass this early period of the crust's history. Indeed, crustal SR (median = 0.37 cm/kyr) do, on average, exceed the ^{230}Th SR (Figure 7a), and the crustal SR distribution is significantly distinct from the ^{230}Th SR distribution ($p = 0.001$, Kolmogorov-Smirnov test). The apparent high SR bias may indicate that the crustal SR is overestimating the true pelagic clay SR over the past several hundred thousands of years.

When ^{230}Th SR and crustal SR are compared on a site-by-site basis (Figure 7b), they are consistent such that higher ^{230}Th SR generally corresponds to higher crustal SR. Unfortunately, the large errors and substantial scatter result in a poor statistical relationship ($R^2 = 0.16$, $p < 0.01$) between the two approaches. The scatter incorporates not only proxy differences but also the real physical processes described above (e.g., pre ^{230}Th time domain depositional history incorporated into crustal SR). A strict 1:1 relationship between the SR cannot realistically be expected, and neither SR estimate represents a "true" or "target" value for the other SR to match. Both proxies should capture relative, broad-scale SR patterns, even if the absolute values of the SRs do not always agree.

A second method for calculating SR is based on the accumulation of non-lithogenic cobalt in sediment (Dunlea, Murray, Sauvage, Pockalny, et al., 2015; Kadko, 1985; Krishnaswami et al., 1976; Zhou & Kyte, 1992). This method assumes that cobalt in the sediment is made of lithogenic cobalt (from dust and volcanic ash) and non-lithogenic cobalt, which is interpreted as cobalt that was formerly in seawater (i.e., hydrogenous cobalt). Some studies have shown that the accumulation rate of non-lithogenic cobalt in slowly accumulating pelagic clays is relatively constant over space and time (Kadko, 1985; Krishnaswami et al., 1976; Manheim, 1986; Manheim & Lane-Bostwick, 1988). Thus, the concentration of non-detrital cobalt is inversely proportional to the accumulation rate of the sediment. Following the approach developed by Dunlea, Murray, Sauvage, Pockalny, et al. (2015) and Dunlea, Murray, Sauvage, Spivack, et al. (2015), we calculate the non-lithogenic cobalt concentrations in each samples using a multivariate statistical calculations, approximated the dry bulk density of 0.4 g of bulk sediment/cm^3, and tested a range ($n = 9$) of predetermined "constant" non-lithogenic cobalt deposition rates (~2–5 μg/cm^2/kyr). This process yields nine estimates of SRs (cm/kyr) for each sample, for which we use the mean and standard deviation (Data Set S4). The uncertainties inherent in this calculation may contribute to real offsets between the cobalt SR and ^{230}Th SR. First, we do not have direct measurements of the dry bulk density for each sample, and this can vary substantially depending on sediment composition, compaction and coring approach. Second, the flux of non-lithogenic cobalt may not be constant in space and time. For example, there appears to be different rates of non-lithogenic accumulation in the Atlantic and the Pacific (Hawco et al., 2018), and within Pacific sediment, the accumulation of non-lithogenic cobalt may be twice as high in the past 5 Myr compared to 5–66 Ma (Kyte et al., 1993). Cobalt fluxes in the Indian Ocean are not constrained. This spatio-temporal variability may be a function of the short residence time of cobalt (~130 years) so that it is not well mixed in the global ocean (Hawco et al., 2018), although the residence time in the deep ocean is long compared to the surface. In relatively old deep waters, Co fluxes become relatively homogenous and may appear constant (Hawco et al., 2018). The Co dating method was intended for very remote regions of the ocean with slowly accumulating sediment, crust, or nodule deposits, but closer to continents, near oxygen minimum zones that supply additional Co (Noble et al., 2012), or in regions with a high biogenic flux, the method may not be as effective. Of the three other SR methods, cobalt has the best agreement with the coretop ^{230}Th/^{232}Th methods in both median value (0.23 cm/kyr) and distribution (no significant difference, $p = 0.38$, Kolmogorov-Smirnov test) (Figure 7a). On a site-by-site basis (Figure 7c), cobalt SR and ^{230}Th SR may appear to fall close to the 1:1 line, ignoring a few outliers, but once again the large errors and substantial scatter result in a poor ($R^2 = 0.10$, $p = 0.01$) statistical relationship between the two approaches.

Figure 7. Comparison of sedimentation rates (SRs) from different methods. Th M3 refers to SRs calculated by method 3. (a) Violin plots depicting the distribution of SR estimates calculated by the various methods. Distributions incorporate the errors in the data. Dark brown lines show the median value. (b)–(d) The coretop ^{230}Th/^{232}Th versus the SRs calculated from (b) age of ocean crust and total sediment thickness, (c) non-lithogenic cobalt-based model, and (d) the global predictive seabed model (GPSM). For subplots (c–d), colorcoding by ocean basin is shown in (b). The dashed line is 1:1 in subplots b–d, and it is provided for reference and not as an expectation. The horizontal bars show 1 standard deviation.

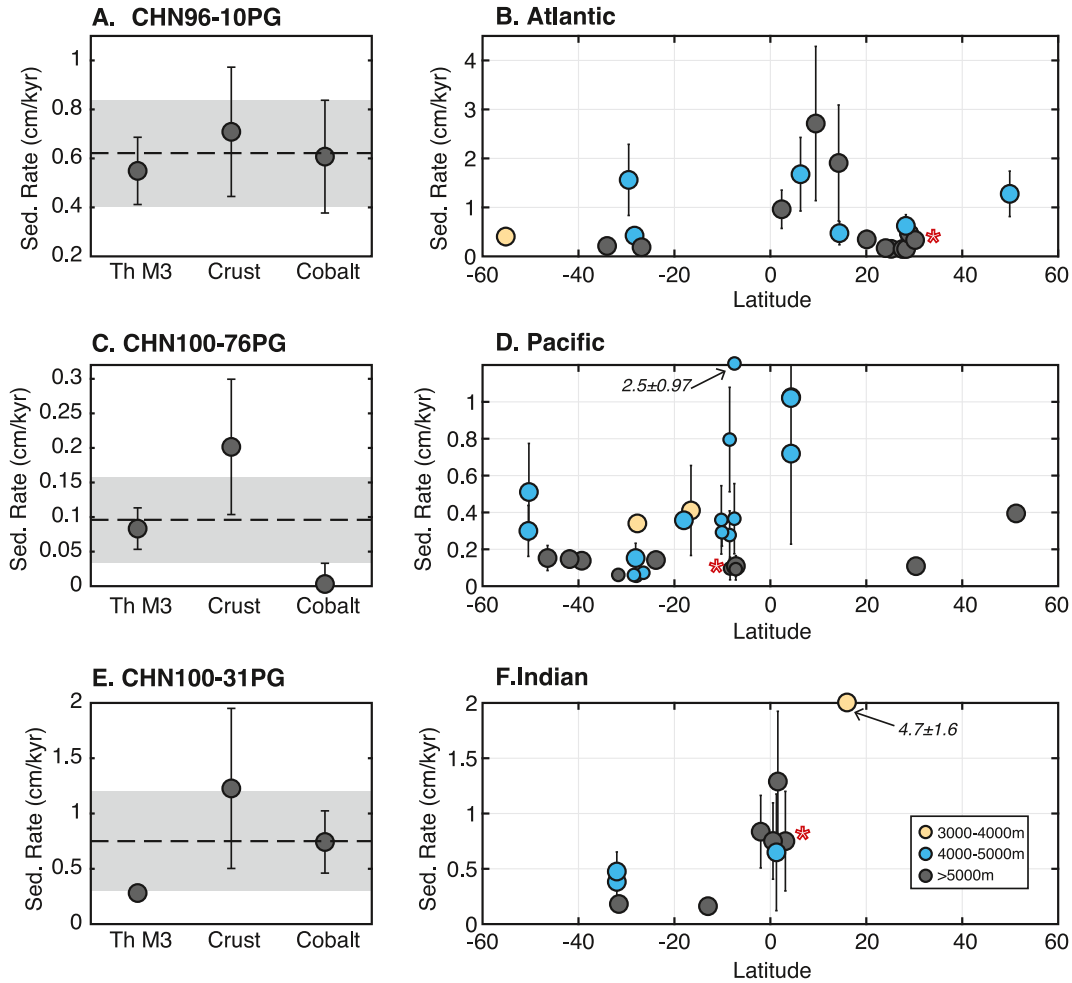

Figure 8. Best estimates of sedimentation rates (SRs). Example cores from the Atlantic (a), Pacific (c), and Indian (e). All three are from depths 5,000–5,150 m. The dashed black line is the final SR, and the shaded region is 1 standard error. Note the different SR scales for each panel. Spatial presentation of the final best SR is shown in the Atlantic (b), Pacific (d), and Indian (f) Oceans. Red stars indicate the example cores shown in panels (a, c, and e), respectively. Two outliers are off the *y*-axis range and superimposed on the figure with their true value reported in the adjacent text. Legend in panel (f) applies to all panels.

Finally, SR has been estimated using a Global Predictive Seabed Model (GPSM) to link discrete SR observations to predictor parameters in order to extrapolate those relationships on a global scale (Restreppo et al., 2020). GPSM SR (and their errors) were calculated on a gridded field that was then interpolated onto the individual sites in this study. The model is best constrained on the continental margins, where there is high data density and where the dynamic range of SR is large. As a result, the most important predictors are skewed toward coastal processes, such as total suspended solids and dissolved organic carbon in river mouths, which would not be relevant in predicting SR in the open ocean. In the remote open ocean, the most relevant predictors were sea surface particulate inorganic carbon, total sediment thickness on the crust, sea surface biomass, seafloor salinity, and sea surface wave direction (Restreppo et al., 2020). The model's optimization toward high SR regions may result in overestimation of SR at our open ocean sites (Figure 7a). Relative to all other methods, the average GPSM SR (median 0.68 cm/kyr) is higher, and the GPSM SR distribution is significantly different ($p < 0.01$, Kolmogorov-Smirnov test) from not only the $^{230}Th/^{232}Th$ method but also from the cobalt and the crust SR distributions.

The structural model skew toward high SR regions also results in low SR having higher uncertainties that can approach 100% (e.g., 0.25 ± 0.19 cm/kyr). The GPSM SRs (Figure 7d) do not demonstrate an apparent relationship with ^{230}Th SR ($R^2 = 0.07$, $p = 0.04$). The systematic bias toward high SR combined with the large

uncertainties at low SR suggest that the GPSM SR may not be an appropriate comparison for the ^{230}Th SR in this study.

Because the accuracy of each proxy at capturing the "true" SR is unknown, combining the information from multiple methods will likely provide the most realistic SR estimate. To calculate a single best estimate of SR at each site, the new (method 3) thorium SR were combined with the crust SR and the cobalt SR to determine a mean SR (Data Set S4). Combining the SR estimates does not change the big picture patterns of sedimentation on the seafloor (Figure 8). The Pacific still has lower SR than the Atlantic or Indian Oceans, and the Sargasso Sea and the South Pacific still have relatively low and uniform SRs. High SR tends to occur along the equator in all three ocean basins. What has changed are the absolute SR values; incorporating our new SRs from core top thorium isotopes as well as cobalt accumulation has revised SRs downward in oxic pelagic clay regions relative to previous SRs derived from crustal estimates (Figures 8a, 8c, and 8e). In some cases, the change in SR is minimal, with core top thorium, cobalt, and crust SRs all agreeing within 95% confidence interval (Figure 8a), but in other cases the crustal SR may have been too high by a factor of two (Figure 8c). While the uncertainties on these SRs are not trivial, they are an honest reflection of our current limitations in geochemical techniques, and further research will only help to improve precision in the future.

5. Conclusions

In this study, we have generated new estimates of SRs in a global suite of oxic pelagic core tops based on their authigenic ^{230}Th/^{232}Th composition relative to that of seawater. Extracting the authigenic fraction was most successful using the HHAc leaching protocol of Bayon et al., 2002, rather than using HCl, which tended to liberate more lithogenic material. To calculate ages from a single core top measurement, the initial ^{230}Th/^{232}Th was estimated from dissolved seawater thorium isotope measurements using different methods of spatial integration (nearest vs. regional; bottommost vs. linear regression). Applying this technique to pelagic sites in the North Pacific with previously published SR estimates found that the best agreement was achieved with method 3, which used the bottommost value from a regionally averaged water column profile as the relevant initial ^{230}Th/^{232}Th for the core top. Combining the SRs calculated using this new thorium technique, as well as the more established cobalt and crustal approaches provided reasonable best estimates of oxic pelagic clay SRs in our global sample set. SRs of oxic pelagic clays are substantially higher in the Atlantic (median 0.46 cm/kyr) than in the Pacific (median 0.28 cm/kyr), while the Indian Ocean has the highest median SR of all three basins (median 0.75 cm/kyr). The new approach presented here suggests that previous techniques involving interpolation of gridded fields (e.g., total sedimentation on the ocean crust, models extrapolating from sea surface properties) may be overestimating the SRs of oxic pelagic clays on the seafloor.

Data Availability Statement

All elemental and isotopic data are available in the NOAA/WDS-Paleo archive at https://www.ncei.noaa.gov/access/paleo-search/study/39521. The dissolved and particulate thorium isotope data are available at https://doi.org/10.6084/m9.figshare.26044024.v1.

Acknowledgments
This study was funded by NSF-GEO NERC 1948716 to A.D., K.M.C., and S.G. N. and NSFGEO-NERC NE/V004824/1 to M.B.A. We thank Dr. Jianghui Du and one anonymous reviewer for their feedback, which helped to improve this paper. WHOI is located on the unceded ancestral and contemporary lands of the Wampanoag people.

References

Bacon, M. P., & Anderson, R. F. (1982). Distribution of thorium isotopes between dissolved and particulate forms in the deep sea. *Journal of Geophysical Research*, *87*(C3), 2045–2056. https://doi.org/10.1029/JC087iC03p02045

Bayon, G., German, C. R., Boella, R. M., Milton, J. A., Taylor, R. N., & Nesbitt, R. W. (2002). An improved method for extracting marine sediment fractions and its application to Sr and Nd isotopic analysis. *Chemical Geology*, *187*(3–4), 179–199. https://doi.org/10.1016/S0009-2541(01)00416-8

Bostrom, K., Kraemer, T., & Gartner, S. (1973). Provenance and accumulation rates of opaline silica, AI, Ti, Fe, Mn, Cu, Ni and Co in Pacific pelagic sediments. *Chemical Geology*, *11*(2), 123–148. https://doi.org/10.1016/0009-2541(73)90049-1

Boudreau, B. P. (1994). Is burial velocity a master parameter for bioturbation? *Geochimica et Cosmochimica Acta*, *58*(4), 1243–1249. https://doi.org/10.1016/0016-7037(94)90378-6

Burckle, L. H., Dodd, J. R., & Stanton, R. J., Jr. (1980). Diatom biostratigraphy and its relationship to paleomagnetic stratigraphy and molluscan distributions in the Neogene Centerville Beach Section, California. *Journal of Paleontology*, *54*(4), 664–674.

Cheng, H., Lawrence Edwards, R., Shen, C. C., Polyak, V. J., Asmerom, Y., Woodhead, J., et al. (2013). Improvements in ^{230}Th dating, ^{230}Th and ^{234}U half-life values, and U-Th isotopic measurements by multi-collector inductively coupled plasma mass spectrometry. *Earth and Planetary Science Letters*, *371–372*, 82–91. https://doi.org/10.1016/j.epsl.2013.04.006

Chester, R., & Hughes, M. J. (1967). A chemical technique for the separation of ferro-manganese minerals, carbonate minerals, and adsorbed trace elements from pelagic sediments. *Chemical Geology*, *2*, 249–262. https://doi.org/10.1016/0009-2541(67)90025-3

Costa, K. M., Hayes, C. M., Anderson, R. F., Pavia, F. J., Bausch, A., Deng, F., et al. (2020). ^{230}Th normalization: New insights on an essential tool for quantifying sedimentary fluxes in the modern and Quaternary ocean. *Paleoceanography and Paleoclimatology*, *35*(2), e2019PA003820. https://doi.org/10.1029/2019pa003820

Costa, K. M., Pavia, F. J., Piecuch, C. G., McManus, J. F., & Weinstein, G. A. (2024). Pelagic sedimentation rates in the North Pacific using Thorium-230 depth profiling. *Geochimica et Cosmochimica Acta*, *369*, 126–140. https://doi.org/10.1016/j.gca.2023.11.020

Dahl, T. W., Hammarlund, E. U., Anbar, A. D., Bond, D. P. G., Gill, B. C., Gordon, G. W., et al. (2010). Devonian rise in atmospheric oxygen correlated to the radiations of terrestrial plants and large predatory fish. *Proceedings of the National Academy of Sciences*, *107*(42), 17911–17915. https://doi.org/10.1073/pnas.1011287107

D'Hondt, S., Inagaki, F., Zarikian, C. A., Abrams, L. J., Dubois, N., Engelhardt, T., et al. (2015). Presence of oxygen and aerobic communities from sea floor to basement in deep-sea sediments. *Nature Geoscience*, *8*(4), 299–304. https://doi.org/10.1038/ngeo2387

Dickson, A. J. (2017). A molybdenum-isotope perspective on Phanerozoic deoxygenation events. *Nature Geoscience*, *10*(10), 721–726. https://doi.org/10.1038/ngeo3028

Diesing, M. (2020). Deep-sea sediments of the global ocean. *Earth System Science Data*, *12*(4), 3367–3381. https://doi.org/10.5194/essd-12-3367-2020

Dunlea, A. G., Murray, R. W., Sauvage, J., Pockalny, R. A., Spivack, A. J., Harris, R. N., & D'Hondt, S. (2015). Cobalt-based age models of pelagic clay in the South Pacific Gyre. *Geochemistry, Geophysics, Geosystems*, *16*(8), 2694–2710. https://doi.org/10.1002/2015GC005892

Dunlea, A. G., Murray, R. W., Sauvage, J., Spivack, A. J., Harris, R. N., & D'Hondt, S. (2015). Dust, volcanic ash, and the evolution of the South Pacific Gyre through the Cenozoic. *Paleoceanography*, *30*(8), 1078–1099. https://doi.org/10.1002/2015PA002829

Dunlea, A. G., Tegler, L. A., Peucker-Ehrenbrink, B., Anbar, A. D., Romaniello, S. J., & Horner, T. J. (2021). Pelagic clays as archives of marine iron isotope chemistry. *Chemical Geology*, *575*, 120201. https://doi.org/10.1016/j.chemgeo.2021.120201

Dutkiewicz, A., & Müller, R. D. (2022). Deep-sea hiatuses track the vigor of Cenozoic ocean bottom currents. *Geology*, *50*(6), 710–715. https://doi.org/10.1130/G49810.1

Dutkiewicz, A., Müller, R. D., O'Callaghan, S., & Jónasson, H. (2015). Census of seafloor sediments in the world's ocean. *Geology*, *43*(9), 795–798. https://doi.org/10.1130/G36883.1

Dymond, J., Corliss, J. B., Heath, G. R., Field, C. W., Dasch, E. J., & Veeh, H. H. (1973). Origin of metalliferous sediments from the East Pacific Rise. *Earth and Planetary Science Letters*, *19*(1), 75–82. https://doi.org/10.1016/0012-821X(73)90179-9

Fleischmann, S., Du, J., Chatterjee, A., McManus, J., Iyer, S. D., Amonkar, A., & Vance, D. (2023). The nickel output to abyssal pelagic manganese oxides: A balanced elemental and isotope budget for the oceans. *Earth and Planetary Science Letters*, *619*, 118301. https://doi.org/10.1016/j.epsl.2023.118301

Garcia, H. E., Weathers, K., Paver, C. R., Smolyar, I., Boyer, T. P., Locarnini, M. M., et al. (2019). World Ocean Atlas 2018, Volume 3: Dissolved Oxygen, Apparent Oxygen Utilization, and Dissolved Oxygen Saturation. Retrieved from https://archimer.ifremer.fr/doc/00651/76337/

Gardner, W. D., Tucholke, B. E., Richardson, M. J., & Biscaye, P. E. (2017). Benthic storms, nepheloid layers, and linkage with upper ocean dynamics in the western North Atlantic. *Marine Geology*, *385*, 304–327. https://doi.org/10.1016/j.margeo.2016.12.012

Goldberg, E. D., & Koide, M. (1962). Geochronological studies of deep sea sediments by the ionium/thorium method. *Geochimica et Cosmochimica Acta*, *26*(3), 417–450. https://doi.org/10.1016/0016-7037(62)90112-6

Gutjahr, M., Frank, M., Stirling, C. H., Klemm, V., van de Flierdt, T., & Halliday, A. N. (2007). Reliable extraction of a deepwater trace metal isotope signal from Fe-Mn oxyhydroxide coatings of marine sediments. *Chemical Geology*, *242*(3–4), 351–370. https://doi.org/10.1016/j.chemgeo.2007.03.021

Hawco, N. J., Lam, P. J., Lee, J.-M., Ohnemus, D. C., Noble, A. E., Wyatt, N. J., et al. (2018). Cobalt scavenging in the mesopelagic ocean and its influence on global mass balance: Synthesizing water column and sedimentary fluxes. *Marine Chemistry*, *201*, 151–166. https://doi.org/10.1016/j.marchem.2017.09.001

Hayes, C. T., Anderson, R. F., Fleisher, M. Q., Huang, K., Robinson, L. F., Lu, Y., et al. (2015). ^{230}Th and ^{231}Pa on GEOTRACES GA03, the U.S. GEOTRACES North Atlantic transect, and implications for modern and paleoceanographic chemical fluxes. *Deep-Sea Research Part II*, *116*, 29–41. https://doi.org/10.1016/j.dsr2.2014.07.007

Hayes, C. T., Anderson, R. F., Fleisher, M. Q., Serno, S., Winckler, G., & Gersonde, R. (2013). Quantifying lithogenic inputs to the North Pacific Ocean using the long-lived thorium isotopes. *Earth and Planetary Science Letters*, *383*, 16–25. https://doi.org/10.1016/j.epsl.2013.09.025

Hayes, C. T., Anderson, R. F., Fleisher, M. Q., Vivancos, S. M., Lam, P. J., Ohnemus, D. C., et al. (2015). Intensity of Th and Pa scavenging partitioned by particle chemistry in the North Atlantic Ocean. *Marine Chemistry*, *170*, 49–60. https://doi.org/10.1016/j.marchem.2015.01.006

Hayes, C. T., Anderson, R. F., Jaccard, S. L., François, R., Fleisher, M. Q., Soon, M., & Gersonde, R. (2013). A new perspective on boundary scavenging in the North Pacific Ocean. *Earth and Planetary Science Letters*, *369–370*, 86–97. https://doi.org/10.1016/j.epsl.2013.03.008

Hayes, C. T., Costa, K. M., Anderson, R. F., Calvo, E., Chase, Z., Demina, L. L., et al. (2021). Global ocean sediment composition and burial flux in the deep sea. *Global Biogeochemical Cycles*, *35*(4), 1–25. https://doi.org/10.1029/2020GB006769

Hein, J. R., Koschinsky, A., Bau, M., Manheim, F. T., Kang, J.-K., & Roberts, L. (1999). Cobalt-rich ferromanganese crusts in the Pacific. In D. S. Cronan (Ed.), *Handbook of marine mineral deposits* (pp. 239–279). CRC Press.

Innocent, C. (2008). Intercomparaison de quatre standards isotopiques de Th synthetises au brgm Premiers resultats. *Rapport BRGM/RP-56066-FR. 36 p., 7 ill.* Retrieved from https://infoterre.brgm.fr/rapports/RP-56066-FR.pdf

Johnson, D., Hooper, P., & Conrey, R. (1999). XRF Analysis of rocks and minerals for major and trace elements on a single low dilution Li-tetraborate fused bead. *JCPDS-International Center for Diffraction Data. Bibliografía Página*, *139*, 843–867.

Kadko, D. (1985). Late Cenozoic sedimentation and metal deposition in the North Pacific. *Geochimica et Cosmochimica Acta*, *49*(3), 651–661. https://doi.org/10.1016/0016-7037(85)90160-7

Krishnaswami, S. (1976). Authigenic transition elements in Pacific pelagic clays. *Geochimica et Cosmochimica Acta*, *40*(4), 425–434. https://doi.org/10.1016/0016-7037(76)90007-7

Krishnaswami, S., Lal, D., Somayajulu, B. L. K., Weiss, R. F., & Craig, H. (1976). Large-volume in-situ filtration of deep Pacific waters: Mineralogical and radioisotope studies. *Earth and Planetary Science Letters*, *32*(2), 420–429. https://doi.org/10.1192/bjp.111.479.1009-a

Ku, T.-L., Broecker, W. S., & Opdyke, N. D. (1968). Comparison of sedimentation rates measured by paleomagnetic and the ionium methods of age determination. *Earth and Planetary Science Letters*, *4*, 1–16. https://doi.org/10.1016/0012-821X(68)90046-0

Kyte, F. T., Leinen, M., Ross Heath, G., & Zhou, L. (1993). Cenozoic sedimentation history of the central North Pacific: Inferences from the elemental geochemistry of core LL44-GPC3. *Geochimica et Cosmochimica Acta*, *57*(8), 1719–1740. https://doi.org/10.1016/0016-7037(93)90109-A

Lam, P. J., Lee, J. M., Heller, M. I., Mehic, S., Xiang, Y., & Bates, N. R. (2018). Size-fractionated distributions of suspended particle concentration and major phase composition from the U.S. GEOTRACES Eastern Pacific Zonal Transect (GP16). *Marine Chemistry*, *201*, 90–107. https://doi.org/10.1016/j.marchem.2017.08.013

Leinen, M. (1987). The origin of paleochemical signatures in North Pacific pelagic clays: Partitioning experiments. *Geochimica et Cosmochimica Acta*, *51*(2), 305–319. https://doi.org/10.1016/0016-7037(87)90243-2

Little, S. H., Archer, C., McManus, J., Najorka, J., Wegorzewski, A. V., & Vance, D. (2020). Towards balancing the oceanic Ni budget. *Earth and Planetary Science Letters*, *547*, 116461. https://doi.org/10.1016/j.epsl.2020.116461

Little, S. H., Vance, D., Walker-Brown, C., & Landing, W. M. (2014). The oceanic mass balance of copper and zinc isotopes, investigated by analysis of their inputs, and outputs to ferromanganese oxide sediments. *Geochimica et Cosmochimica Acta*, *125*, 673–693. https://doi.org/10.1016/j.gca.2013.07.046

Longhurst, A. (1995). Seasonal cycles of pelagic production and consumption. *Progress in Oceanography*, *36*(2), 77–167. https://doi.org/10.1016/0079-6611(95)00015-1

Manheim, F. T. (1986). Marine cobalt resources. *Science*, *232*(4750), 600–608. https://doi.org/10.1126/science.232.4750.600

Manheim, F. T., & Lane-Bostwick, C. M. (1988). Cobalt in ferromanganese crusts as a monitor of hydrothermal discharge on the Pacific sea floor. *Nature*, *335*(6185), 59–62. https://doi.org/10.1038/335059a0

Marchig, V., Gundlach, H., Möller, P., & Schley, F. (1982). Some geochemical indicators for discrimination between diagenetic and hydrothermal metalliferous sediments. *Marine Geology*, *50*(3), 241–256. https://doi.org/10.1016/0025-3227(82)90141-4

McCave, I. N. (1986). Local and global aspects of the bottom nepheloid layers in the world ocean. *Netherlands Journal of Sea Research*, *20*(2–3), 167–181. https://doi.org/10.1016/0077-7579(86)90040-2

Mikhailik, P. E., Khanchuk, A. I., Mikhailik, E. V., Rashidov, V. A., Savelyev, D. P., & Zarubina, N. V. (2023). Ferromanganese crusts of the North Pacific Ocean. *Russian Journal of Pacific Geology*, *17*(2), 101–133. https://doi.org/10.1134/S1819714023020045

Miyake, Y., & Sugimura, Y. (1961). Ionium-thorium chronology of deep-sea sediments of the Western North Pacific. *Science*, *133*(3467), 1823–1824. https://doi.org/10.1126/science.133.3467.1823

Müller, R. D., Sdrolias, M., Gaina, C., & Roest, W. R. (2008). Age, spreading rates, and spreading asymmetry of the world's ocean crust. *Geochemistry, Geophysics, Geosystems*, *9*(4), Q04006. https://doi.org/10.1029/2007GC001743

Nielsen, S. G., Rehkämper, M., Porcelli, D., Andersson, P., Halliday, A. N., Swarzenski, P. W., et al. (2005). Thallium isotope composition of the upper continental crust and rivers - An investigation of the continental sources of dissolved marine thallium. *Geochimica et Cosmochimica Acta*, *69*(8), 2007–2019. https://doi.org/10.1016/j.gca.2004.10.025

Noble, A. E., Lamborg, C. H., Ohnemus, D. C., Lam, P. J., Goepfert, T. J., Measures, C. I., et al. (2012). Basin-scale inputs of cobalt, iron, and manganese from the Benguela-Angola front to the South Atlantic Ocean. *Limnology and Oceanography*, *57*(4), 989–1010. https://doi.org/10.4319/lo.2012.57.4.0989

Nozaki, Y., Yang, H.-S., & Yamada, M. (1987). Scavenging of thorium in the ocean. *Journal of Geophysical Research*, *92*(C1), 772–778. https://doi.org/10.1029/jc092ic01p00772

Okubo, A., Obata, H., Gamo, T., & Yamada, M. (2012). ^{230}Th and ^{232}Th distributions in mid-latitudes of the North Pacific Ocean: Effect of bottom scavenging. *Earth and Planetary Science Letters*, *339–340*, 139–150. https://doi.org/10.1016/j.epsl.2012.05.012

Opdyke, N. D., & Foster, J. H. (1970). Paleomagnetism of cores from the North Pacific. *Memoir of the Geological Society of America*, *126*, 83–119. https://doi.org/10.1130/MEM126-p83

Ostrander, C. M., Owens, J. D., & Nielsen, S. G. (2017). Constraining the rate of oceanic deoxygenation leading up to a Cretaceous Oceanic Anoxic Event (OAE-2: ∼94 Ma). *Science Advances*, *3*(8), e1701020. https://doi.org/10.1126/sciadv.1701020

Pavia, F. J. (2024). Seawater Thorium isotope database [Dataset]. *Figshare*. https://doi.org/10.6084/m9.figshare.26044024.v1

Pavia, F. J., Anderson, R. F., Vivancos, S., Fleisher, M., Lam, P., Lu, Y., et al. (2018). Intense hydrothermal scavenging of ^{230}Th and ^{231}Pa in the deep Southeast Pacific. *Marine Chemistry*, *201*, 212–228. https://doi.org/10.1016/j.marchem.2017.08.003

Peucker-Ehrenbrink, B., Ravizza, G. E., & Hofmann, A. W. (1995). The marine ^{187}Os/^{186}Os record of the past 80 million years. *Earth and Planetary Science Letters*, *130*(1–4), 155–167. https://doi.org/10.1016/0012-821X(95)00003-U

Potter, E.-K., Stirling, C. H., Andersen, M. B., & Halliday, A. N. (2005). High precision Faraday collector MC-ICPMS thorium isotope ratio determination. *International Journal of Mass Spectrometry*, *247*(1–3), 10–17. https://doi.org/10.1016/j.ijms.2005.08.017

Raiswell, R., Canfield, D. E., & Berner, R. A. (1994). A comparison of iron extraction methods for the determination of degree of pyritisation and the recognition of iron-limited pyrite formation. *Chemical Geology*, *111*(1–4), 101–110. https://doi.org/10.1016/0009-2541(94)90084-1

Restreppo, G. A., Wood, W. T., & Phrampus, B. J. (2020). Oceanic sediment accumulation rates predicted via machine learning algorithm: Towards sediment characterization on a global scale. *Geo-Marine Letters*, *40*(5), 755–763. https://doi.org/10.1007/s00367-020-00669-1

Robinson, L. F., Noble, T., & McManus, J. F. (2008). Measurement of adsorbed and total ^{232}Th/^{230}Th ratios from marine sediments. *Chemical Geology*, *252*(3–4), 169–179. https://doi.org/10.1016/j.chemgeo.2008.02.015

Rowland, G. H., Chin, H., Robinson, L. F., Mcmanus, J. F., Mohamed, K. J., & McGee, D. (2017). Investigating the use of ^{232}Th/^{230}Th as a dust proxy using co-located seawater and sediment samples from the low-latitude North Atlantic. *Geochimica et Cosmochimica Acta*, *214*, 143–156. https://doi.org/10.1016/j.gca.2017.07.033

Rudnick, R. L., & Gao, S. (2003). Composition of the continental crust. In *Treatise on Geochemistry* (Vol. 3, pp. 1–64). https://doi.org/10.1016/b0-08-043751-6/03016-4

Straume, E. O., Gaina, C., Medvedev, S., Hochmuth, K., Gohl, K., Whittaker, J. M., et al. (2019). GlobSed: Updated total sediment thickness in the world's oceans. *Geochemistry, Geophysics, Geosystems*, *20*(4), 1756–1772. https://doi.org/10.1029/2018GC008115

Trauth, M. H. (2013). TURBO2: A MATLAB simulation to study the effects of bioturbation on paleoceanographic time series. *Computers & Geosciences*, *61*, 1–10. https://doi.org/10.1016/j.cageo.2013.05.003

Uramoto, G. I., Morono, Y., Tomioka, N., Wakaki, S., Nakada, R., Wagai, R., et al. (2019). Significant contribution of subseafloor microparticles to the global manganese budget. *Nature Communications*, *10*(1), 1–10. https://doi.org/10.1038/s41467-019-08347-2

Van Hulten, M., Middag, R., Dutay, J. C., De Baar, H., Roy-Barman, M., Gehlen, M., et al. (2017). Manganese in the west Atlantic Ocean in the context of the first global ocean circulation model of manganese. *Biogeosciences*, *14*(5), 1123–1152. https://doi.org/10.5194/bg-14-1123-2017

Zhou, L., & Kyte, F. T. (1992). Sedimentation history of the South Pacific pelagic clay province over the last 85 million years inferred from the geochemistry of Deep Sea Drilling Project Hole 596. *Paleoceanography*, *7*(4), 441–465. https://doi.org/10.1029/92PA01063

References From the Supporting Information

Albani, S., Mahowald, N. M., Perry, A. T., Scanza, R. A., Zender, C. S., Heavens, N. G., et al. (2014). Improved dust representation in the Community Atmosphere Model. *Journal of Advances in Modeling Earth Systems*, *6*(3), 541–570. https://doi.org/10.1002/2013MS000279

Anderson, R. F., Cheng, H., Edwards, R. L., Fleisher, M. Q., Hayes, C. T., Huang, K., et al. (2016). How well can we quantify dust deposition to the ocean? *Philosophical Transactions. Series A, Mathematical, Physical, and Engineering Sciences*, *374*(2081), 20150285. https://doi.org/10.1098/rsta.2015.0285

Chen, T., Zheng, J., Li, T., Shi, X., Robinson, L. F., Wang, M., et al. (2023). Thorium isotope evidence for glacial–interglacial dust storminess and productivity in the North Pacific gyre. *Geochimica et Cosmochimica Acta*, *346*, 15–28. https://doi.org/10.1016/j.gca.2023.01.007

Deng, F., Thomas, A. L., Rijkenberg, M. J. A., & Henderson, G. M. (2014). Controls on seawater ^{231}Pa, ^{230}Th and ^{232}Th concentrations along the flow paths of deep waters in the Southwest Atlantic. *Earth and Planetary Science Letters*, *390*, 93–102. https://doi.org/10.1016/j.epsl.2013.12.038

Hsieh, Y.-T., Henderson, G. M., & Thomas, A. L. (2011). Combining seawater ^{232}Th and ^{230}Th concentrations to determine dust fluxes to the surface ocean. *Earth and Planetary Science Letters*, *312*(3–4), 280–290. https://doi.org/10.1016/j.epsl.2011.10.022

Kienast, S. S., Winckler, G., Lippold, J., Albani, S., & Mahowald, N. M. (2016). Tracing dust input to the global ocean using thorium isotopes in marine sediments: ThoroMap. *Global Biogeochemical Cycles*, *30*(10), 1526–1541. https://doi.org/10.1002/2016GB005408

Koschinsky, A., & Hein, J. R. (2003). Uptake of elements from seawater by ferromanganese crusts: Solid-phase associations and seawater speciation. *Marine Geology*, *198*(3–4), 331–351. https://doi.org/10.1016/S0025-3227(03)00122-1

Liu, R., Wang, M., Li, W., Shi, X., & Chen, T. (2020). Dissolved thorium isotope evidence for export productivity in the subtropical North Pacific during the late Quaternary. *Geophysical Research Letters*, *47*(11), 1–9. https://doi.org/10.1029/2019GL085995

Lopez, G. I., Marcantonio, F., Lyle, M., & Lynch-Stieglitz, J. (2015). Dissolved and particulate ^{230}Th-^{232}Th in the Central Equatorial Pacific Ocean: Evidence for far-field transport of the East Pacific Rise hydrothermal plume. *Earth and Planetary Science Letters*, *431*, 87–95. https://doi.org/10.1016/j.epsl.2015.09.019

Pavia, F. J., Anderson, R. F., Winckler, G., & Fleisher, M. Q. (2020). Atmospheric dust inputs, iron cycling, and biogeochemical connections in the South Pacific Ocean from thorium isotopes. *Global Biogeochemical Cycles*, *34*(9), 1–18. https://doi.org/10.1029/2020GB006562

Winckler, G., Anderson, R. F., Fleisher, M. Q., McGee, D., & Mahowald, N. (2008). Covariant glacial-interglacial dust fluxes in the equatorial Pacific and Antarctica. *Science*, *320*(5872), 93–96. https://doi.org/10.1126/science.1150595